RSC Sustainability

Accepted Manuscript

This article can be cited before page numbers have been issued, to do this please use: J. Cherusseri, S. A. Thomas and D. N. Rajendran, *RSC Sustainability*, 2025, DOI: 10.1039/D5SU00085H.

ROYAL SOCIETY OF CHEMISTRY

View Article Online
DOI: 10.1039/D5SU00085H

Sustainability spotlight

The current energy demand requires sustainable and renewable electrochemical energy storages devices that have features such as mobility, high specific energy, low cost, and safe. Electrochemical energy storage devices such as rechargeable batteries and supercapacitors utilize nanostructured electrode-active materials for their charge storage. Metallenes-based electrodes become a versatile option to develop sustainable batteries and supercapacitors. These devices achieve the UN Sustainable Development Goal 7: Affordable and Clean Energy. Metallenes-based electrodes may conquer the world of sustainable electrochemical energy storage devices as they are robust, stable, low-cost, high performance and safe to use.

Ultrathin 2D Metallenes for Energy Storage: A Myth or Reality?

View Article Online
DOI: 10.1039/D5SU00085H

Jayesh Cherusseri[1*], Susmi Anna Thomas[2], and Deepthi N. Rajendran[2]

[1]Department of Chemistry (BK21 FOUR), Research Institute of Advanced Chemistry, Gyeongsang National University, Jinju 52828, Republic of Korea
[2]Department of Physics, Government College for Women (Affiliated to University of Kerala), Thiruvananthapuram, Kerala 695014, India

***Corresponding Author**
E-Mail Address: drjayeshpuli@gmail.com (Jayesh Cherusseri)

Abstract

Rapid depletion in fossil fuel and increased energy scarcity paved the way to utilize electrochemical energy storage device like rechargeable batteries and supercapacitors to power electronic devices. Ultrathin two-dimensional (2D) materials attract great research interest due to their prominent characteristics like large surface area, lightweight, good electronic conductivity, good chemical and electrochemical properties, etc. to name a few. Metallenes are emerging class of 2D materials having atomic thickness and consisting of metals or alloys with a well-controlled surface atomic arrangement. 2D metallenes are invariably used as electrode-active materials in energy storage devices such as rechargeable batteries and supercapacitors in the literature. Since metallenes consist of metallic 2D sheets, the charge storage is limited by the electrode kinetics and also more prone to corrosion when used in electrolytes, this motivated us to examine the truth behind these fascinating materials. We critically analyse the various types of metallenes available to date, their synthesis methods and the mechanism of charge storage in rechargeable batteries and supercapacitors for a better clarification.

Keywords: 2D materials, Metallenes, Supercapacitors, Rechargeable batteries, Density Functional Theory

1. Ultrathin 2D Metallenes

Ultrathin two-dimensional (2D) layered materials received significant research interest due to their large surface area, suitable plane for charge-transfer and quantum-size effect [1-4]. After the discovery of graphene, the research has been carried out to synthesize various types of 2D materials where the conductivity spans from insulator to semiconductor toward conductors [5-7]. 2D materials are different from their bulk counterparts in terms of properties [8, 9]. The peculiar properties of 2D materials such as physical, chemical, optical, electronic, thermal, and mechanical properties enabled them to utilize in a variety of applications including catalysis, energy storage, sensors, etc [10, 11]. There are almost hundreds of 2D materials are explored to date and some examples are transition metal dichalcogenides [12-14], layered double hydroxides [15], graphitic carbon nitride [16], MXenes [17, 18], etc. In the literature, the materials ended with “ene” refers to ultrathin 2D materials. For example, borophene, silicene, germanene (Ge-ene), phosphorene, stanene (Sn-ene), antomonene (Sb-ene), bismuthine (Bi-ene), etc. to name few. Among these, silicene and phosphorene are semiconductors whereas borophene, Ge-ene, Sn-ene, Sb-ene, and Bi-ene are considered metallenes. A "metallene" is a hypothetical class of materials that would be analogous to graphene but are composed of metals or alloys. Metallenes are good conductors of electricity with thickness in the range of one or several atomic layer.

View Article Online
DOI: 10.1039/D5SU00085H

In comparison with other metals which are widely using, metallenes have high conductivity hence are promising materials for catalysis, supercapacitors, batteries, etc [19]. Beyond other non-2D materials and bulk counterpart of metals, metallenes possess extraordinary properties ranging from conductivity to superconductivity[20]. Atomically thin architecture of metallenes exhibits large surface area to volume ratio, which helps in coordinating with other atoms by unsaturated metal atom present on the surface and edge sites. In comparison with surface atom, coordinated edge atoms found to be unsaturated due to the formation of defects, dislocation, etc., hence achieves high electrochemical activity for electrochemical energy storage [21-23]. Metallenes hold higher percentage of surface unsaturated metal sites that behaves as the active sites, making it as an efficient candidate, particularly in energy storage applications [9]. Higher specific surface area and increased surface energy possessed by metal atom promote adsorption mechanisms hence are suitable for ubiquitous charge storage. The ultrathin feature of metallenes gives rise to reducing the diffusion distance of electrolyte-ions in the electrolyte medium. Beyond these features, the capability for surface functionalization metallenes envisage us to tune their electronic structure, electrochemical stability, hydrophilicity, etc [14].

Although metallenes possess several advantages, the research on metallenes is still in infancy. The thermodynamic instability and limited synthesis routes available make their application limited. Hence, to obtain a free-standing layer remains a challenge in the case of metallenes[24]. In order to demonstrate the wide range of acceptability in proposed metallenes as an ultrathin material for energy storage applications, we are planned to write this review in order to make the truth behind acceptability of this class of materials. A statistical representation of number of citations related to metallenes is given in **Figure 1**. The number of citations received for the publications for each year is given as an inset graph of **Figure 1**. From this graphical representation, it can be observed that there exists only very small number of publications and studies with respect to metallenes in the literature but a rapid increase in research related to metallenes can be viewed for the past 5 years.

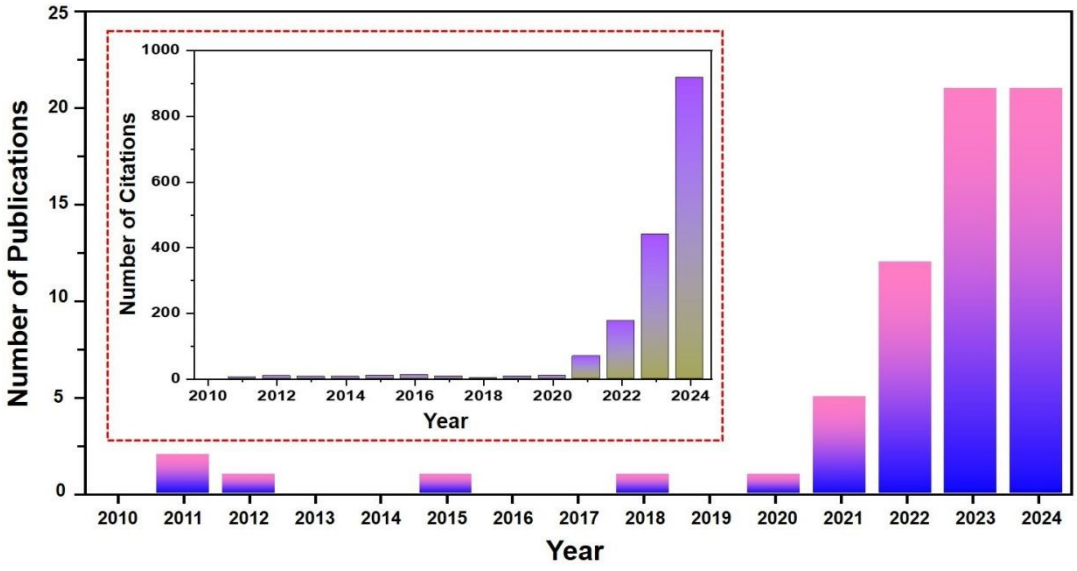

Figure 1. The number of publications (Inset: number of citations received in each year) related to metallenes for past 15 years (Source: Web of Science; Keyword: "Metallenes").

Depletion of fossil fuel resources and the ever-increasing global population led to severe energy crisis. Although various renewable energy conversion technologies are developed such as solar cells, wind mills, tidal turbines, their intermittent nature necessitates

View Article Online
DOI: 10.1039/D5SU00085H

the need of energy storage technologies. Among the various choices available, the most promising energy storage is the electrochemical energy storage. This includes capacitors, batteries, and supercapacitors. Conventional capacitors or dielectric capacitors are good candidates with high-power density but very low energy density. On the other hand, supercapacitors exhibit high specific capacitance, high power density and moderate energy density. Batteries are the most common examples for electrochemical energy storage devices that we use in our daily life. Rechargeable batteries such as metal-ion batteries[25], metal-sulfur batteries[26], and metal-air batteries[27] are the mostly explored battery types. Electrode and electrolyte materials play a crucial role in determining the voltage window and electrochemical performance of batteries and supercapacitors [28, 29]. Detailed reviews on various advanced materials for application in energy storage are available in the literature. But the salient features of using 2D metallenes in energy storage is not explored to date. This has motivated us to ask a research question: "ultrathin 2D metallenes for energy storage is a myth or reality?". This review critically evaluates the salient features of metallenes capable to use in energy storage applications such as in supercapacitors and batteries. We review the fundamental properties of metallenes along with their synthesis routes and their exemplary application in the field of energy storage.

2. 2D Metallenes for Supercapacitors

There are different types of metallenes explored to date, most of them are explained theoretically and only a small number experimentally. After the discovery of graphene in the year 2004, it became a fascinating material of choice for many of the electronic device applications due to their tunability in the electronic structure, number of layers, surface functionalization, etc. Graphene and graphene derivatives are invariably used in energy storage due to their unique features such as 2D architecture, large surface area, good chemical and electrochemical stabilities, good capacity, etc [30]. Graphene is a perfect choice for semiconducting devices whereas the metallenes are not suitable due to their zero bandgap [31]. However, ligand-functionalized metallenes may be complimentary to graphene in the future [32]. Ge-ene-based materials received prominent attention in the field of energy storage, particularly for electric double layer capacitors (EDLCs). Similar to graphene, a monolayered Ge-ene holds a honeycomb buckling structure, which can store charges by the formation of double layer, studied theoretically. Researchers have carried out simulation studies such as, hydrogenation, functionalization, organic functional group termination, exogenous doping of elements, etc. From these studies, it is observed that the physical and chemical features of Ge-ene can be altered [19]. A recent study comprising of experimental and theoretical analysis of low-dimensional materials such as carbon nanotube and graphene unveils the overall interface capacitance is a series combination of a double-layer capacitance and quantum capacitance (C_Q) [33]. From this study, it is clear that C_Q have significant influence on the total capacitance. At a reduced applied potential, C_Q of graphene limits the performance of EDLC. A variation in the C_Q affects the overall capacitance of the electrode-active material. Xu et al. [33] evaluated C_Q of pristine and defect-induced Ge-ene through first principle calculations with the aid of projected augmented wave potential approach with Vienna Ab initio Simulation Package. In this study, the exchange correlation energy of the interacting electron is obtained by a generalized gradient approximation functional with Perdew-Burke-Ernzerhof (PBE) functional. Here, integral k-space and the plane wave basis set having a cut off energy of 450 eV is selected properly for making overall convergence of energy at 1 meV/level. Here, Monkhorst–Pack having higher k-point density is utilized to evaluate k-points in the Brillouin region. Using sp^3/sp^2 hybridization, buckled honeycomb structure hold by Ge-ene holds a lattice constant of 3.84 Å with a Ge–Ge bond length of 2.268 Å. The authors of this work observed that the pristine Ge-ene exhibits linear dispersion near to Fermi level having Dirac

View Article Online
DOI: 10.1039/D5SU00085H

point same as that of graphene. A Stone-Wales defect (SW defect) makes Ge-ene to have a linear dispersion near to Fermi level, which breaks a degenerate state near Γ region. In comparison with density of states of bulk Ge-ene, for SW defect, there exist a peak positioned at 0.3 eV above the Fermi level (or the Dirac point) through introduction of SW flat bands. These flat bands and degenerated states breaking near to Γ reveals that there exists a partial distortion in network of state from the Ge atom p(z) hybridization. Thereby it produces a quasi-localization state near to SW defect. The injected charge carriers gather near to Ge ring pentagon-heptagon, it is introduced from decomposed band charge density isosurfaces. Moreover, a state near to Γ point indicates a higher number of additional charges distributed in the Ge crystal lattice. The C_Q of pristine and the six different defective Ge-ene electrodes are further evaluated at a temperature of 300K and shown in **Figure 2a-f**. The C_Q profile of each Ge-ene electrode is similar to density of states shape in thermal broadening. The C_Q is increased with an increase in $|\Phi|$ and it reaches to 60 μF cm^{-2} at $\Phi = \pm 0.6$ V for the pristine Ge-ene. Beyond this, for the all six defect-induced Ge-ene electrodes, a higher irregular C_Q is observed near to neutrality point. The C_Q of pristine Ge-ene makes a significant increase and this peak corresponds to the above-mentioned quasi-localized p(*z*) state. In this present point of view, the overall accumulation of charge (**Figure 2g** and **h**) DV defects V_2 (9–4–9) and the V_2 (5–4–5) holds an increase in effect during a positive bias, but with a negative bias, the accumulation of charges increases rapidly for defects V_2 (5555–6–7777), V_2 (5–8–5) and the SW defect.

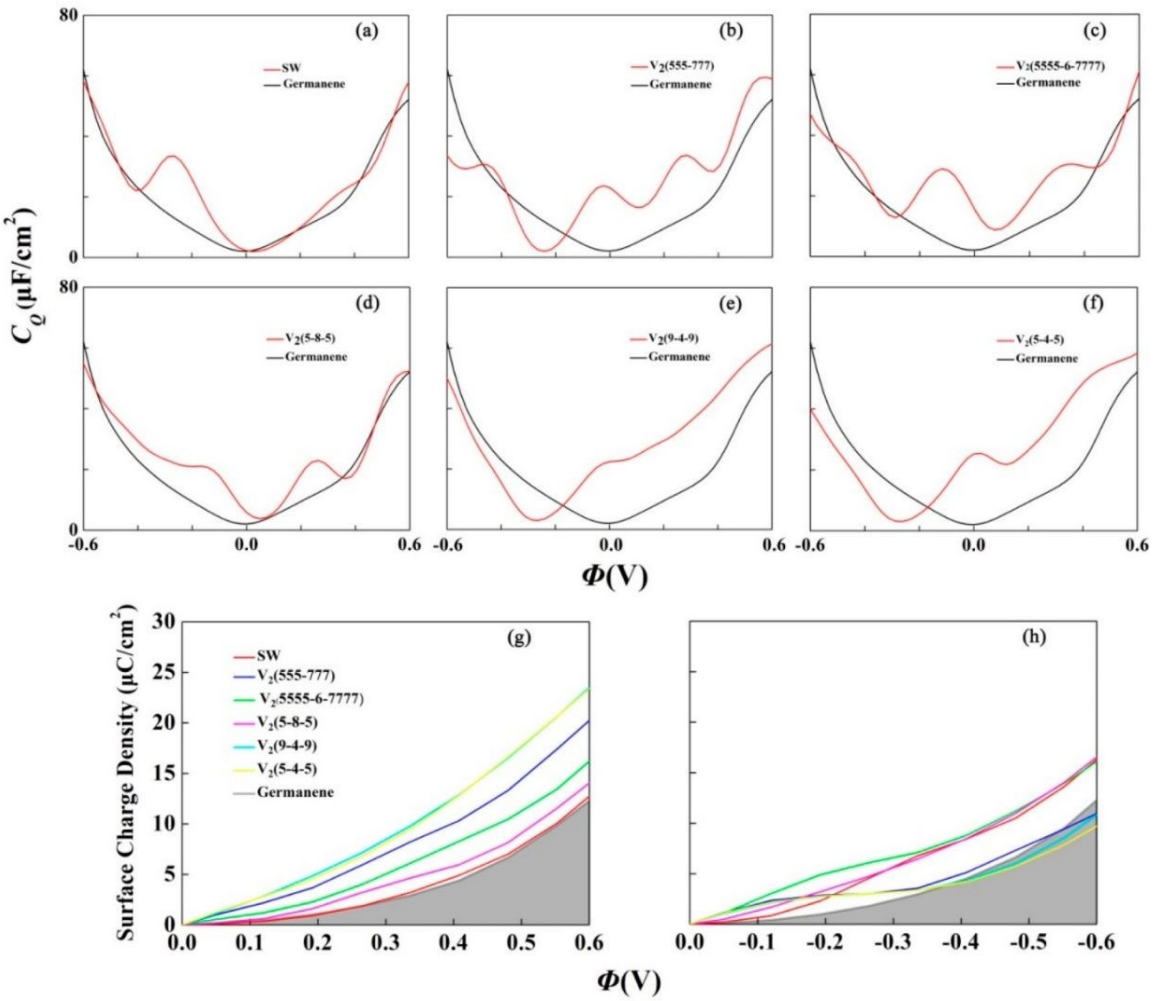

Figure 2. (a-f) C_Q for pristine Ge-ene defective Ge-ene; (g, h) surface charge density variation with respect to potential drop having Φ in the range −0.6 to 0.6 V. The results are evaluated in

View Article Online
DOI: 10.1039/D5SU00085H

the supercell 6 x 6 and it possess a defect concentration of 1.39%. Reproduced with permission from [33] Copyright (2020) American Chemical Society.

To evaluate the electronic structure of metal doped Ge-ene, charge density isosurface with band decomposed of Ti and Cu doping was analysed. For states occupied with energy level between the -0.5 eV and the Fermi level, the distribution of charges is intensive over Ti (Cu) atom and nearby Ge three atoms. In doping Ti, these proposed states are coming from Ge p(z) and the Ti 3d(z^2) orbital contribution. In doping Cu, this given states are introduced from the Cu 3d(x^2–y^2) and the Ge 4p orbital consists of p(x), p(y) and p(z). If band make an occupied state above Fermi level and smaller than by value 0.5 eV, given charge also make distribution mainly over Ti (Cu) atom having nearby Ge atoms in complex. In Ti doping, it shows two group of localized bands. The localized band near to Fermi level is from the Ge p(z) and Ti d(xy)/d(x^2–y^2) orbital contribution. Here, the second group present in localized band are introduced from the Ti d(z^2) orbital. With similarity to metal atom doped graphene, overlap exists between Ge quasi-sp^2 and the Ti d(xz)/d(yz) orbitals out-of-plane resulting to σ–σ* states (σ is from Ge p(x)/p(y) and σ* is from Ti d(xz) and Ti d(yz)). In Cu doping, the Fermi level is shifting down clearly with respect to Cu 3d electron deficiency. The Cu 3d orbital doesn't hold any contribution from conduction band it comes specifically from π* state of Ge p(z) orbital. For adsorption of Cu atom on pristine Ge-ene, charges make a transfer from the Cu to Ge atom and it localized at a region near to three atoms in upper surface having higher symmetry, but for the Cu doping having SV Ge-ene, introduction of chemical bonds present between the Cu and the Ge atoms. In electrode's operation state, stability of system about metal adsorption on bare Ge-ene is changed by following injection/removal of electron, because this stability is controlled by transfer of charges. With respect to the removal of electron in the operation, there exists a reduction in transfer of charges, and there is a decrease in adsorption stability. During metal adsorption on SV Ge-ene, stability doesn't make any prominent changes in operation state with respect to the orbital hybridization as primary factor. Influence of Ge-ene SV with respect to various metal adsorbates depends upon C_Q is analysed in **Figure 3a**. To analyse effect of the doping on C_Q, here value of this quantum capacitance corresponds to pristine and doped Ge is shown in the **Figure 3a**. In case of SV Ge-ene, the C_Q value of pristine Ge-ene make an improvement. This is by the presence of localized state near to Dirac point generated by metal dopant complex and SV. For examine localization effect of states near to Fermi energy of doped system is evaluated by the temperature dependency of C_Q as shown in **Figure 3b**. By changing temperature of system in the range 0 to 400 K, they evaluated the value of C_Q at zero bias. For present case, they observed that pristine Ge-ene doesn't show any changes and it hold a value of ~1.96 μF cm^{-2}. For system Au,Ti, Cu, Ag and Al combined with SV, there is no prominent change in C_Q with respect to the temperature. With respect to the local electrode potential function, a change in C_Q of the Ti- and the SV with Cu-doped, Ge-ene having various concentration is shown in **Figure 3c** and **d**. By increasing the concentration of Ti from the 2% to 8.3%, C_Q increase from 48.9 μF cm^{-2} (−0.14 V) towards 141.1 μF cm^{-2} (−0.38 V). In comparison with pristine Ge-ene, electronic structure hold by Ge-ene is not affected through reduced concentration of dopant Ti. For 5.6% doping concentration, C_Q hold a maximum value of 110.2 μF cm^{-2} at a temperature of 300 K in Ti-doped Ge-ene (**Figure 3c**). C_Q with respect to Φ at various concentration is evaluated, for a reduced concentration, localized energy state is introduced through the defects which begins to hybridize and expanding by quasi-localization.

View Article Online
DOI: 10.1039/D5SU00085H

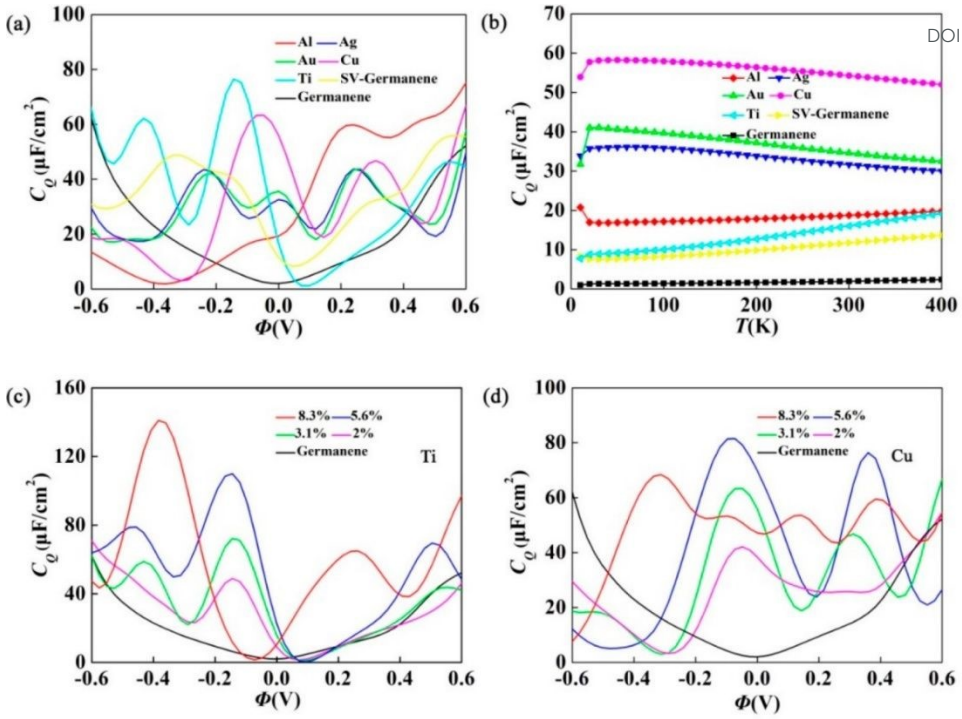

Figure 3. (a) calculated C_Q of the SV Ge-ene with given elements adsorbed and the SV Ge-ene with respect to local electrode potential (Φ); (b) change in C_Q with temperature range of 0-400 K; calculated C_Q of SV Ge-ene with respect to (c) Ti and (d) doping of Cu having concentration of 2%, 3.1%, 5.6%, and 8.3% with respect to local electrode potential. Reproduced with permission from [33] Copyright (2020) American Chemical Society.

Stanene (Sn-ene) is another member in the family, composed of single layer of tin (Sn) atoms are arranged in a 2D manner. Sn-ene exhibits prominent features like room temperature spin hall quantum effect, the topological superconductivity behaviour, and the thermoelectricity, etc. to name a few [34]. Sn-ene monolayer can be prepared over $Bi_2Te_3(111)$ through molecular beam epitaxy[34]. Alloy terminated surface is found to be a template for the growth of higher scale Sn-ene film. Zhou et al. [35] studied about the influence of vacancy-defect, doping of single element and co-doping on C_Q of Sn-ene electrode material. The authors selected two different types of dopants such as: light-element dopants like B, N, Al, Si, P and S and the transition-metals such as Ti, V, Cr, Mn, Fe and Ni. Their studies showed that Sn-ene exhibits high C_Q under vacancy at 0 V. The capacitance is found to be increased with co-doping in comparison with single-atom doping. Sn-ene with co-doped atomic framework possesses an efficient C_Q for negative potential than positive bias, suggests that it act as an effective cathode material for supercapacitors. Partial density of states results suggests that C_Q curve shifting mainly due to the contribution from transition metal, the light element dopant, and the Sn atom and this study suggests that Sn-ene-based electrodes are efficient candidates for supercapacitor application.

Antimonene (Sb-ene) is an another important metallene, which has received great interest for electrochemical applications due to its isolation from the conventional layered allotrope form. It is possible to synthesize few-layered Sb-ene through liquid phase exfoliation [36]. There is a modified synthesis approach which involves an initial step which treated with a ball-milling approach carried out at 3000 rpm for a milling period of 180 minutes. In the initial step, it involves a prominent reduction in size of Sb crystals and the homogenous maintenance of this size. Using SEM imaging it is confirmed that prepared Sb power possesses a uniformity in structure. To evaluate the electrochemical charge storage properties of this

View Article Online
DOI: 10.1039/D5SU00085H

powder, Sb modified screen-printed electrode (SPE) is characterized using SEM analysis. SEM image shows that Sb forms flakes that hold a lateral dimension of ~200-400 nm. The supercapacitor performance of this prepared electrode is evaluated in a two-electrode cell configuration with 0.5 M H_2SO_4 electrolyte. The authors of his work have observed reduction and oxidation peaks in the cyclic voltammetry (CV) curves, which is due to the oxidation and reduction of Sb-ene, due to Faradaic phenomena, contributes to the total capacitance. The supercapacitor electrode prepared with 36 ng of Sb-ene exhibited a specific capacitance of 1578 F g^{-1} at a current density of 14 A g^{-1}. The charge/discharge stability of this electrode undergoes 10000 galvanostatic charge/discharge (GCD) cycles and achieved good capacitance retention. The supercapacitor delivered an energy density 20 mW h kg^{-1} at a corresponding power density of 4.8 kW kg^{-1} [37].

A high-performing supercapacitor with bismuthine (Bi-ene)/Sb-ene was synthesized through the injection of interaction between adjacent layers through hydrogen bonding, the van der Waals force, and the covalent bond [38] . The covalent bond between these two metallenes provide efficient combined dynamics and structural stability, which induced through standard liquid-phase exfoliation approach. A hybrid supercapacitor was assembled using Bi-ene/Sb-ene as positive electrode and the activated carbon (AC) as negative electrode. The SEM image of Bi-ene represents the presence of 3D microspheres holding a rough morphology with an average particle size of 400 nm. Exfoliated Bi-ene exhibits thin nanosheets were laterally aligned with a mean lateral dimension of 120 nm. SEM image of bulk Sb holds large number of cubic nanocrystals having smooth surface and its diameter varied between 300 to 500 nm. Exfoliated Sb-ene have large nanosheets which are randomly stacked having smooth surface with a mean sheet length of 80 nm. There exists a random distribution of Bi-ene and Sb-ene nanosheets having perfectly defined sheet boundaries with surfaces having smooth morphology with a mean sheet diameter of ~100 nm. An asymmetric hybrid supercapacitor with Bi-ene/Sb-ene as positive and AC as negative electrode was assembled having optimized potential window of −1.0 - 0.0 V and 0.0 - 0.6 V, for positive and negative electrodes respectively. The CV curves obtained at a scan rate of 10 mV/s is shown in **Figure 4a**. The hybrid supercapacitor achieved an operating potential window of 0.0 - 1.5 V and the CV curves obtained at different scan rates is depicted in **Figure 4b**. Since the hybrid supercapacitor utilizes both an EDLC electrode and a pseudocapacitive electrode, the net charge storage is a combination of both the mechanisms. Since the positive electrode having a 2D nanostructure, a battery-type charge storage is anticipated since a higher degree of intercalation/deintercalation of electrolyte-ions between Bi-ene/Sb-ene interlayers is possible that gives rise to an enhancement in charge storage. This in turn enhances the ionic conductivity thereby a higher electrochemical activity towards charge storage may happen. A large area under a CV curve is an indication of higher charge storage as the area under the curve is directly proportional to the specific capacitance. The high electronic conductivity of the Bi-ene/Sb-ene electrodes is responsible for the high-rate performance of the hybrid supercapacitor. The Nyquist plot of the hybrid supercapacitor along with the equivalent circuit model fitted is given in **Figure 4c**, which reveals low charge transfer resistance hence high ionic conductivity and faster ion diffusion kinetics. The series resistance (R_s) and charge transfer resistance (R_{ct}) calculated for the hybrid supercapacitor and found to be 0.438 and 3.372 Ω, respectively. The GCD curves obtained at different current densities for the hybrid supercapacitor is depicted in **Figure 4d**. This hybrid supercapacitor exhibited a specific capacity of 560 and 176 C g^{-1} at a current density of 2 and 10 A g^{-1}, respectively. This supercapacitor exhibited a capacitive retention of 86.2% after 3000 charge/discharge cycles with a Coulombic efficiency of 124.12%, as shown in **Figure 4e**. The supercapacitor also delivered an energy density of 131.44 Wh kg^{-1} with a maximum power density of 8262.2 W kg^{-1}, evident from the Ragone plot (**Figure 4f**) [38].

View Article Online
DOI: 10.1039/D5SU00085H

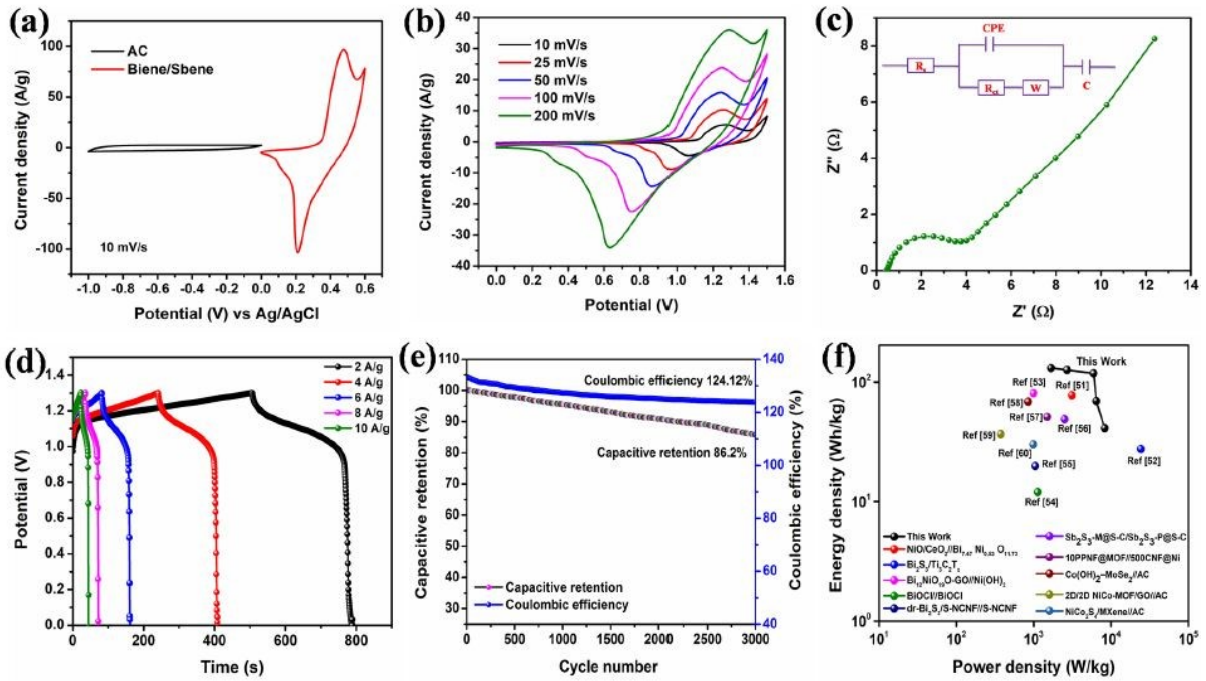

Figure 4. (a) CV curves of AC and Bi-ene and Sb-ene at 10 mV/s scan rate; (b) CV curves of HSC at different scan rates; (c) Nyquist plot (inset: equivalent circuit); (d) GCD profiles of HSC at different current densities; (e) Capacitive retention and Coulombic efficiency of HSC; (f) Comparison of energy and power density of prepared HSC with other reports in the literature. Reproduced with permission from [38] Copyright (2022) American Chemical Society.

Mariappan et al. [39] introduced a 3D nickel core (Ni) comprising of Sb-ene dendrite having hierarchical structure by electrochemical deposition technique. The Sb-ene particles dispersed over the Ni foam surface uniformly after an electrochemical deposition period of 5 s. A further increase in the deposition time such as, 10 and 15 s resulted in the generation of dendritic nanostructures of Sb-ene with varied densities. The electrochemical performance of the supercapacitor electrode synthesized at a deposition period of 15 s exhibited a higher specific capacitance although the electrode constitutes dense dendritic structure. The electrochemical performances of the electrode material are evaluated in a two-electrode cell arrangement using Sb-ene/Ni as the positive electrode and graphene as the negative electrode in 1 M LiOH aqueous electrolyte. The CV analyses shows that there is no distortion to the curves even at higher scan rates, indicates its efficient ionic and electronic conductivity. The asymmetric supercapacitor possessed a specific capacitance of 172.6 F g^{-1} at a scan rate of 5 mV s^{-1} and delivered a higher energy density of 84.79 Wh kg^{-1} with a corresponding power density of 20.6 kW kg^{-1}.

3. 2D Metallenes for Rechargeable Batteries

Layered metallenes have significant advantages for rechargeable batteries, due to their good structural stability, large surface area, and fast intercalation/deintercalation of ions between layers, etc. Efficient synthesis of 2D metallenes such as Ge-ene, silicene and Sn-ene have profound interest for rechargeable batteries. Sharma et al. [40] evaluated the electrochemical performance of monolayered and the bi-layered Ge-ene as anode for Li-ion batteries (LIBs) using first-principle calculation with DFT. The authors of this work have observed a single atom Li adsorption on monolayered Ge-ene. Here, the Li adatom located at the hexagonal ring

View Article Online
DOI: 10.1039/D5SU00085H

H-site having three near neighbour Ge atoms with a bond length of ~2.70 Å. The formation energy in this particular direction is equal to −0.43 eV. For the adsorption with two Li atoms, there is two chances; first one is the adsorption of both of these two atoms of Li above Ge-ene or one is above and other below Ge-ene. In the second case, the calculated formation energy is −0.54 eV, which is smaller by 0.04 eV with respect to the first one. Thus, adsorption of greater than one Li atom over Ge-ene is more favourable. To evaluate the adsorption of Li in bilayer Ge-ene, they evaluated the same as like as monolayer one. For the single atom case, Li atom is adsorbed in the hexagon structure H-site, delivers a formation energy of -0.75 eV. By increasing the number of atoms, this formation energy increases than single atom adsorption of Li and attains a value of -0.70 eV for two atoms. Further increasing the number of atoms to 4, 8 and 12, the formation energy becomes −0.74, −0.79, and −0.64 eV respectively. Using this theoretical approximation, they found that monolayer and bilayer Ge-ene is covered with a number of Li-ions. By the increase in atoms, there exists a pushing of nearby Ge atoms by new Li atoms that creates a lattice distortion. In order to reduce the distortion of lattice, the particular adatom is placed above the favourable adsorption site than film. In accordance to increase in number of atoms it creates large number of electronic charges all around Ge atoms of Ge-ene. In the case of completely lithiated monolayer and bilayer Ge-ene, there exists a repulsion for further adsorption of Li atom and it gets stabilized. Therefore, the overall energy hold by the system is moved toward a higher value. With the aid of this theoretical calculation, they found that Li adsorbed monolayer and bilayer Ge-ene hold a specific capacity of 369 and 276 mA h g^{-1}, respectively. A layered and stable Ge-ene hydride (GeH) was synthesized by large-scale route of exfoliation and purification approach for utilizing as anode material in LIBs [41]. Here $CaGe_2$ was synthesized under Ar atmosphere for minimizing water concentration and oxidation. Stoichiometric quantity for Ge and calcium granules was homogeneously mixed through ball-milling. The resultant powder is loaded to an Al crucible and it is sealed in quartz ampule under vacuum. The prepared samples are annealed at a melting point greater than individual binary elements at a temperature of 1000ºC for 24 h and further allowed to cool to room temperature. The prepared product is intercalated with HCl at a temperature of −20ºC for a duration of 5 days in order to prepare a layered GeH. The stacked Ge layered structure is shown in **Figure 5a**. X-ray diffraction (XRD) analysis of $CaGe_2$ agrees with JCPDS Card No. #00-013-0299. There exists calcium oxide and germanium impurities through higher reactivity hold by calcium having trace quantity of oxygen at an elevated temperature. Calcium oxide can easily be removed by subsequent etching with HCl. The XRD spectrum of layered GeH (**Figure 5b**) exhibits a peak positioned at 2θ value of ~15.4º corresponds to (002) peak, which indicates interlayer spacing of 5.7 Å. Also, spectrum shows some indication for the crystalline Ge. SEM image of GeH powder reveals a layered architecture having width in the range of ~1 μm, as shown in **Figure 5c**.

View Article Online
DOI: 10.1039/D5SU00085H

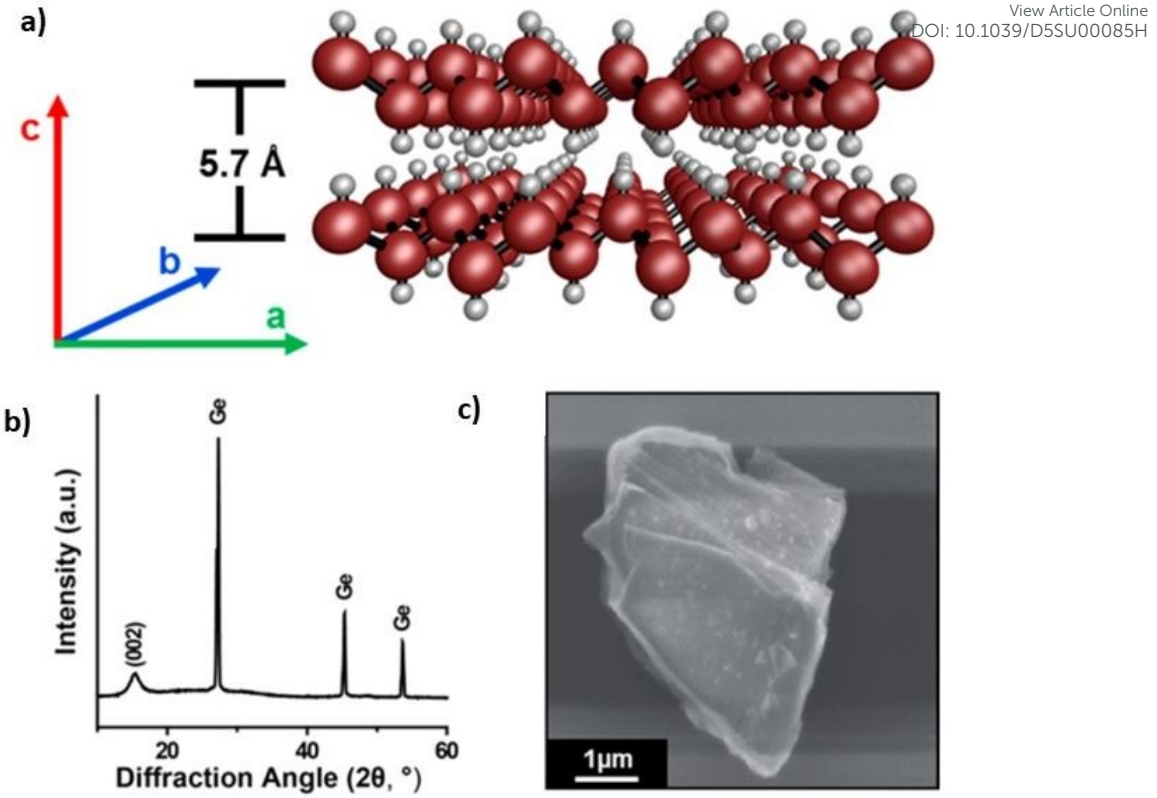

Figure 5. (a) Pictorial representation for stacked structure of Ge; (b) XRD spectrum of Ge with stacking peak present at ~15.4º, the other peaks represent characteristic Ge elemental impurities; (c) SEM image of Ge. Reproduced with permission from [41] Copyright (2017) American Chemical Society.

The micro and nanoscale characteristics of solution exfoliated GeH sheets and its degree of exfoliation and degradation were measured. Exfoliated GeH sheets are tends to aggregate when it is in the dry state and shows prominent reduction in the lateral size through force introduced during ultrasonication. Transmission electron microscopy (TEM) imaging shows that GeH exfoliated sheets tends to aggregate during evaporation of solvent, there exists a reduced number of the isolated single sheets. Here, the polydispersed solution contain apparent single sheets ranging in the lateral dimension of 40 - 200 nm and the stacked sheets are ranging from 40 nm to 1 µm. The authors have used GeH in LIBs by preparing composite with carbon in order to reduce the solid electrolyte interphase (SEI) layer formation as well as to increase the electronic conduction. After performing exfoliation, carbon nanofibers and carbon black were added to the GeH dispersion. The carbon nanofibers provide large surface area and carbon black helps in increasing the electronic conductivity. The as-prepared mixture is sonicated at a temperature of 15ºC for a duration of 30 minutes and the resultant black product is drop-casted and kept for drying. After preparing the slurry, the oxygen atoms present in poly(acrylic acid) facilitates hydrogen bonding between binder and hydrogen on surface of GeH. This prepared slurry is later introduced to stainless-steel mesh which possesses an area of 0.5 x 0.5 cm^2, and kept for drying under vacuum at room temperature for 12 h. This fabricated electrode was folded itself and further pressed under a force of 10000 lbs, which results in an electrode thickness <0.2 mm. The GeH mixture mass loading on electrodes was ~3-5 mg cm^{-2}. The control sample is prepared in a similar manner with pure Ge powder with carbon nanofibers and carbon black. The electrochemical analysis is performed in an Ar-filled glovebox having oil mixture at O level <1 ppm. The cycling study for LIB is performed with $LiClO_4$ (1.0 M) in

View Article Online
DOI: 10.1039/D5SU00085H

a 95:5 mixture of anhydrous propylene carbonate and fluoroethylene carbonate. By using anhydrous fluoroethylene carbonate as an additive, it provides an enhancement in SEI layer stability. Here, Li metal is utilized as reference and auxiliary electrodes. The CV curves of exfoliated GeH and bulk Ge anodes at a scan rate of 0.1 mV/s obtained for the second cycle is given in **Figure 6a**. There exists two characteristics with the lithiation process; a broader peak present at ~0.3 V and a steady increasing current at a low potential which terminate at the cutoff voltage of 0.1 V vs. Li/Li$^+$. The delithiation process is represented with broader peak observed between 0.4 and 0.6 V vs. Li/Li$^+$. This peak corresponds to the formation of several Ge_xLi_y phases generated during insertion/deinsertion of Li. The Ge lithiation follows **equation 1**, and there exists several steps for lithiation, occurs at different electrochemical potential. The entire crystalline $Li_{15}Ge_4$ lithiation results to amorphous Ge. A similar feature can be observed in the second CV cycle of the GeH and the bulk Ge.

$$Ge + Li \xrightarrow{Lithiation} Li_{15}Ge_4 \xrightarrow{Delithiation} Ge_{amorphous} + Li \ldots (1)$$

A confocal *ex situ* Raman spectroscopy is utilized to demonstrate the changes in structural GeH after performing the electrochemical cycling study, given in **Figure 6b**. Here, GeH pristine anode possesses a characteristic peak located at 227.1 and 302.3 cm^{-1}, corresponds to A_1 out-of-plane and the E_{2g} in-plane vibration of Ge. A broader peak located at ~526 cm^{-1} attributes to $(Ge{-}H)_w$ vibrational mode of hydrogen. There exists an absence of hydrogen bending at ~800 cm^{-1} or the stretching mode observed at 1890 and 1975 cm^{-1}. After completing the cycling study, the Raman spectrum of GeH anode makes a prominent change in which A_1 out-of-plane and the E_{2g} in-plane vibration of Ge broadens and shift toward 269.5 cm^{-1}. There exists a disappearing in wag of hydrogen bond at ~526 cm^{-1}, which indicates hydrogen removal through Li alloying. During this lithiation and delithiation process there exists a change in structural pattern, represents crystalline order of Ge changed to amorphous. The GCD measurements (**Figure 6c** and **d**) were performed to calculate the capacity hold by composite anode of GeH/carbon matrix at different cycling rates. For second cycle given in **Figure 6d**, which accurately determine performance of material through multitude side reaction which occurs during charging/discharging. During the initial cycles, a large change was observed in both the specific capacity and the Coulombic efficiency. At a charging rate of C/10, a maximum capacity of 1108 mAh g^{-1} was observed and a reduction in capacity at high rates. The maximum capacity obtained for GeH lithiation and the delithiation having carbon matrix (the black square and red circle, respectively) and the carbon matrix (black and red line, respectively) at different C rates is given in **Figure 6d**. Here, non-zero slope as a cell voltage function represents that it doesn't contain any single-phase transition, instead a range of transition, which is occurred at nanoscale due to the large strain in solid Ge and Si during the lithiation process. An initial capacity of 1533 mAh g^{-1} at a rate of C/10 is higher than the theoretically predicted one for GeH at room temperature. But there exists large capacity distortion is observed due to the electrolyte breakdown and the formation of SEI layer, which clearly shows the irreversible characteristics of the anode. The irreversible redox peaks appeared at 0.54 and the 0.94 with Li/Li$^+$ at a scan rate of 0.1 mV s^{-1} at the first CV cycle for GeH. The disappearance of first reduction peak indicates that hydrogen is introducing to total storage of charge in the first cycle. After few cycles, there exists a stabilization of capacity at ~1110 mAh g^{-1}. It possesses a reduction in overall charge storage in accordance to the increase in rate, having capacity of 893, 720, 530, and 265 mAh g^{-1} for the C/5, C/2, 1C, and 2C, respectively. The loss in capacity at a high charge rate is same as other anodes prepared of Ge, due to the kinetic limitations of the host matrix. There exists a recovery in capacity when rate is returned at C/10. The Coulombic efficiency in the composite anode is stabilized with after performing the first five

View Article Online
DOI: 10.1039/D3SU00085H

cycles and it is averaged to ~98%. The initial reduction in the performance observed at first five cycles is due to the formation of SEI layer.

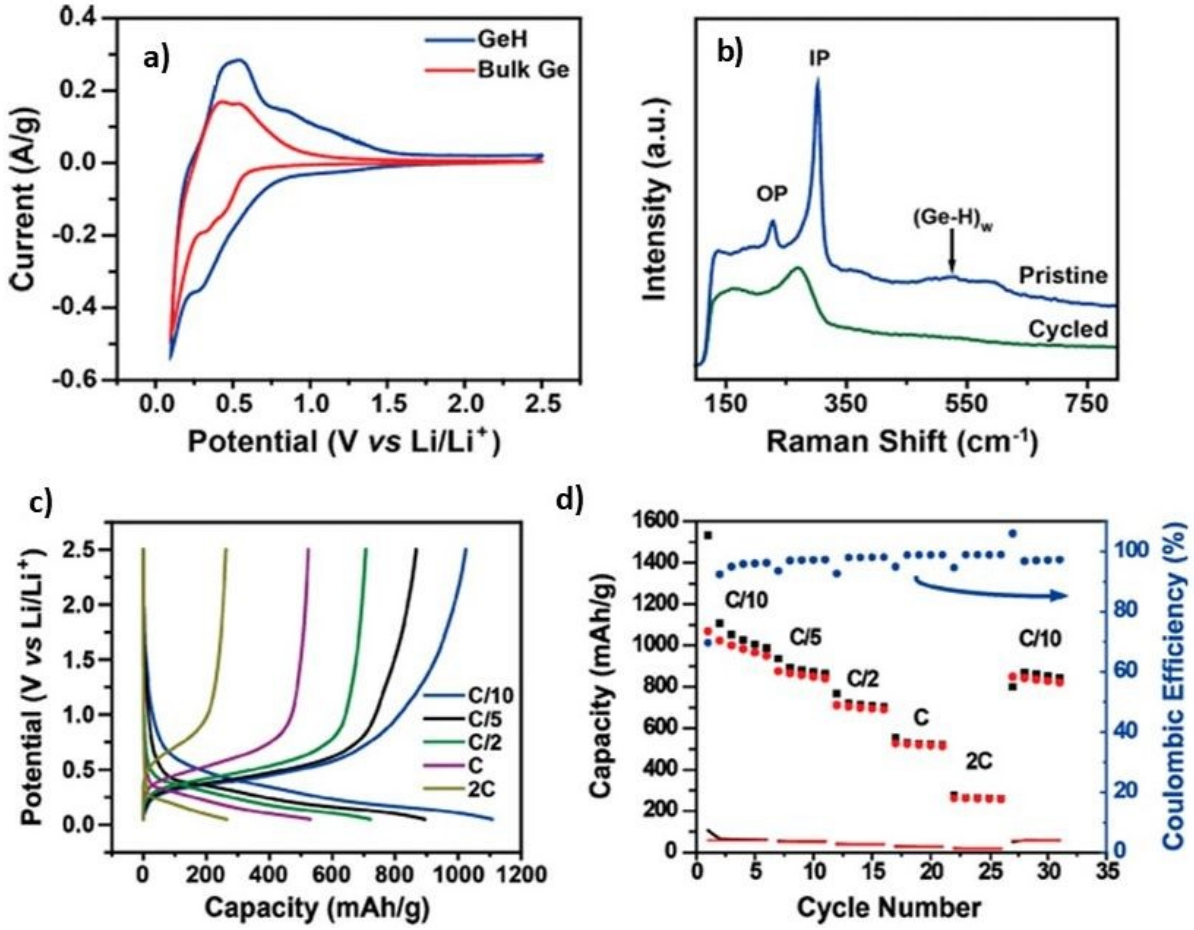

Figure 6. (a) Comparison of CV diagrams for GeH and Ge bulk anode cycled between the potentials 2.5 and 0.1 V at a scan rate of 0.1 mV s^{-1}; (b) *Ex situ* Raman spectra for pristine (blue, top) and the Li-cycled (bottom, green) Ge anode which shows indication for change in structure associated in the delithiation driven of amorphization for GeH sheet; (c) GCD profiles for GeH anode at different charge and discharge rates within a potential window of 0.1 - 2.5 V vs Li/Li^+; (d) insertion and the extraction maximum capacity for GeH anode plotted with black square and the red circle, respectively, having Coulombic efficiency plotted with blue circles. Here, the insertion and extraction capacity contributions from carbon fiber/carbon black/and poly(acrylic acid) binder are plotted in black and red lines, respectively. Reproduced with permission from [41] Copyright (2017) American Chemical Society.

Zhang and team synthesized few layered staene (Sn-ene) quantum dots having lateral size of ~8 nm with a thickness of about 1 nm is self-reconstructed from SnFe-monolayer Prussian Blue analogue nanosheets (SnFe-PBA-NSs) [42]. It is prepared by large scale through a facile ultrasonication controlled self-assembly which is combined through a fluid flow control arrangement. The authors of this work have prepared few layered Sn-ene quantum dots using *in situ* electrochemical reduction approach with SnFe-PBA-NSs as self-sacrificial template. The structural and the morphological features of the prepared SnFe-PBA-NSs were evaluated. XRD analysis revealed that the SnFe-PBA-NSs holds an ultrathin multiply interconnected NSs having lateral diameter in the micrometer scale (**Figure 7a**). The mean thickness of these NSs is measured to be ~1.36 nm, estimated with the help of AFM imaging, in correlation with the

theoretical thickness of 13.6 Å for monolayer $Sn_2[Fe(CN)_6]$, verifies the single layer characteristics of SnFe-PBA-NSs, as given in **Figure 7b** and **c**. The microstructure of SnFe-PBA-NSs was examined using high-resolution TEM (HRTEM) and high-angle annular dark-field scanning transmission electron microscopy (HAADF-STEM). The semi-transparent character in HRTEM image indicates the ultrathin thickness of SnFe-PBA-NSs monolayer and this proposed NSs are found to be interwined (**Figure 7d**). In addition to this, a HRTEM image representing several NSs layers touches closely each other is depicted in **Figure 7e**. The selected area electron diffraction (SAED) pattern shown in the inset graph of **Figure 7e**, indexed as in-plane 2D reflections having zone axis in [001] directions confirm the rhombohedral pattern, agrees with the XRD analysis too. Here, the NSs coordination polymer is sensitive to electron beam, it introduces some degree of lattice distortion. However, the undamaged parts in HRTEM makes a clear display of lattice fringes with an interplanar spacing of 0.364 nm (**Figure 7f**) corresponds to (110) plane of SnFe-PBA. The HAADF-STEM image and the corresponding energy-dispersive spectroscopy (EDS) elemental mapping analysis for the SnFe-PBA-NSs indicates a homogeneous distribution of various elements within the material (**Figure 7g**).

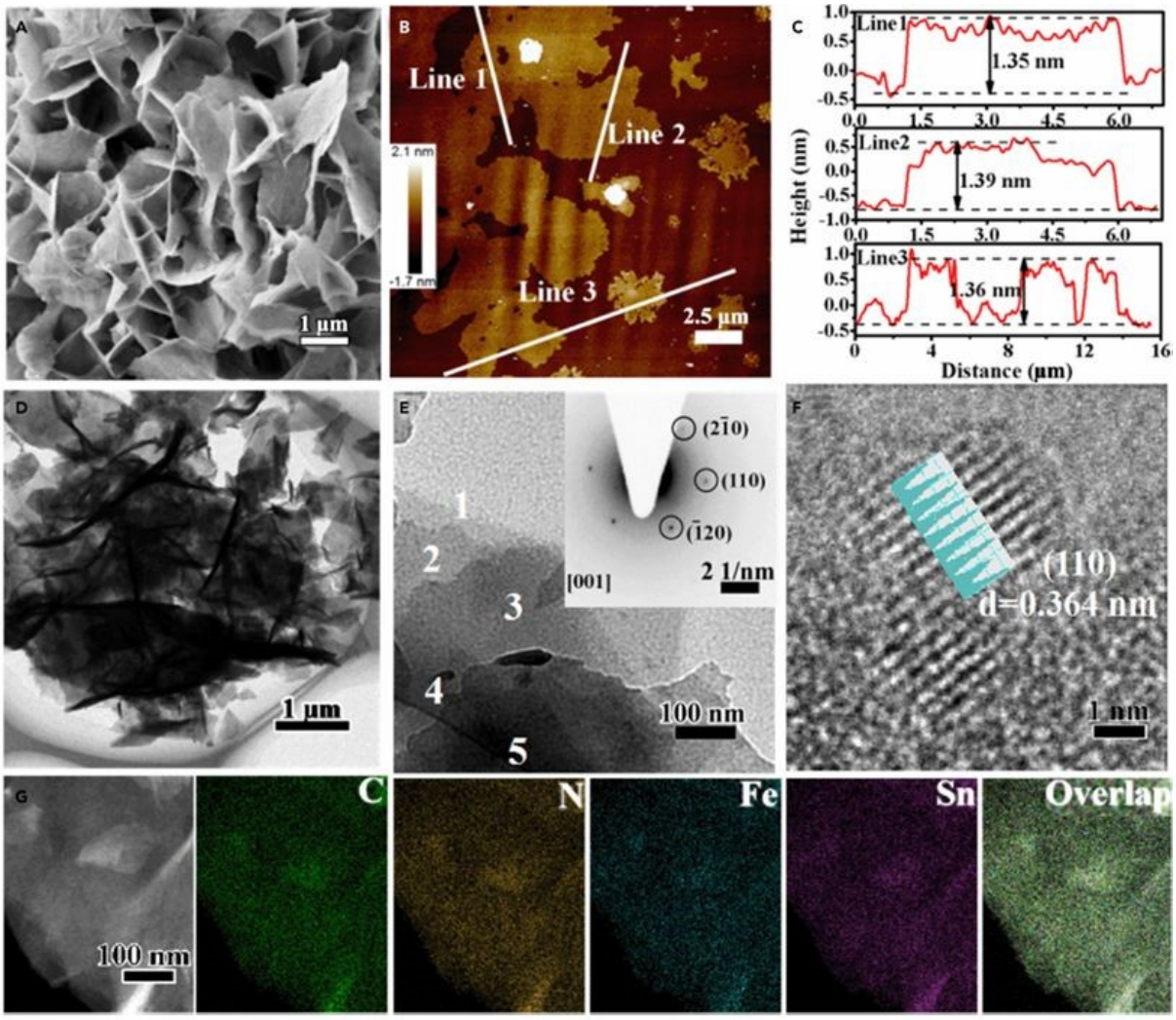

Figure 7. Morphological and microstructural characterizations of SnFe-PBA-NSs. (a) SEM image; AFM image (b) and the corresponding height profiles (c); (d and e) HRTEM images (inset image represents the SAED pattern); (f) HRTEM image showing the lattice fringes; (g)

View Article Online
DOI: 10.1039/D5SU00085H

HAADF-STEM image and the corresponding EDS elemental mapping images. Reproduced with permission from [42] Copyright (2022) Elsevier Inc.

These Sn-ene quantum dots hold features such as abundant exposed active sites, especially edge centres and it possess higher efficiency for fabricating a rechargeable battery. The authors of this work have fabricated a Zn-CO_2 battery system in a flow cell configuration having 0.5 M $KHCO_3$ filled in cathodic compartment which is pumped by CO_2. Here, the anolyte selected was 6 M KOH + 0.02 M $Zn(CH_3COO)_2$. The CO_2 gas flow is controlled using a flow meter in order to make a flow rate through the cathodic compartment at 20 mL min^{-1}. A perfectly polished Zn plate having an area of 2 x 3 cm^2 was used as an anode. With respect to the excellent carbon dioxide redox reaction (CO_2RR) characteristics, the Sn-ene quantum dots served as excellent candidates as a catalyst. The schematic diagram of the Zn-CO_2 battery assembled is shown in **Figure 8a**. The discharge polarization curve along with power density at different current densities is depicted in **Figure 8b**. The Zn-CO_2 battery delivered a maximum power density of 1.25 mW cm^{-2} at a current density of 7.9 mA cm^{-2}. The practical application of this Zn-CO_2 battery is evaluated by connecting two individual batteries connected in series that could power a light emitting diode (LED), as shown in **Figure 8c**. Additionally, the Zn-CO_2 battery holds an excellent cycling stability for more than 560 cycles when performed at a current density of 1 mA cm^{-2} (**Figure 8d**). **Figure 8e** compares the potential of Sn-ene cathode-based Zn-CO_2 battery with the literature, which clearly shows its superior performance.

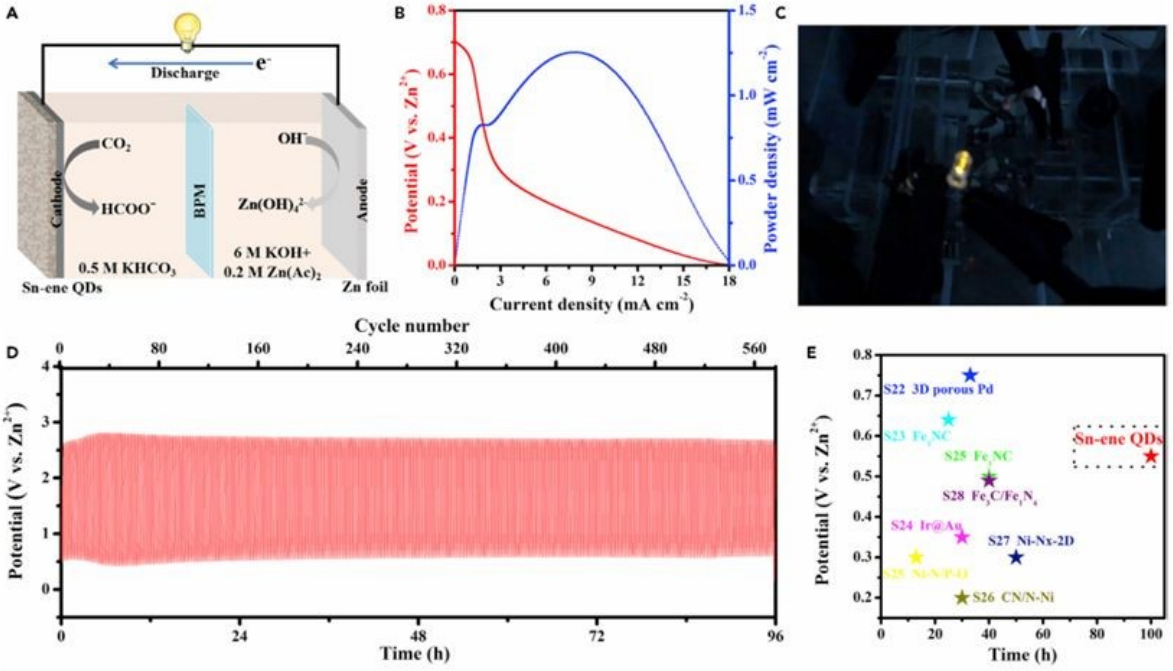

Figure 8. Electrochemical measurements for the Zn-CO_2 battery. (a) Schematic diagram of the battery; (b) the discharge polarization curve and variation of power density with respect to current density; (c) two Zn-CO_2 batteries connected in series powering a LED; (d) Cyclic stability test results for 96 h at a current density of 1 mA cm^{-2}; (e) Comparison of Se-ene cathode-based Zn-CO_2 battery with similar reports in the literature. Reproduced with permission from [42] Copyright (2022) Elsevier Inc.

The sodium-ion batteries (SIBs) are extensively studied candidates among the various rechargeable batteries nowadays due to their high safety, low cost, and environmentally friendly nature [43]. SIBs take advantageous features such as Na resource abundance, reduced

View Article Online
DOI: 10.1039/D5SU00085H

cost and lower reduction potential [44]. There are reports based on metallenes for SIBs, in order to establish its application in rechargeable batteries beyond LIBs. Ge-ene with higher specific surface area buffers the volume expansion in Na-ion charging/discharging. Also, the reduced diffusion path for electrons/ions and efficient mechanical flexibility helps in achieving higher cyclic stability. Due to the defect-rich structure of Gene induces an improved adsorption of Na ion to the active sites, thereby increasing storage capability of SIBs. It is reported that the Ge-ene nanosheets can be synthesized via thermal dehydrogenation of the 2D hydrogenated Ge-ene (GeH) single crystals [45]. In this synthesis approach, the GeH nanosheet precursor is synthesized through the Zintl-phase $CaGe_2$ topochemical intercalation at a reduced temperature range, and it is further annealed at a temperature of 270ºC to remove the H layers. After performing subsequent annealing for 1 h at higher temperature, Ge-ene particles were obtained from Ge-ene nanosheets. The as-prepared GeH nanosheets hold a mean lattice spacing of 0.332 nm. To make a comparison, the authors of this work evaluated the electrochemical characteristics of ultrathin GeH nanosheets, Ge-ene having higher H defects and Ge particles is evaluated in a coin-type half-cell with Na metal foil as a counter electrode. The Na-ion storage characteristics of GeH, Ge-ene nanosheets and Ge particles were characterized using CV analysis at a fixed scan rate of 0.1 mV s^{-1} in 1M $NaClO_4$ electrolyte and the CV curves are shown in **Figure 9a-c** for the GeH, Ge-ene nanosheets and Ge particles, respectively. The initial cathodic curves of all the Ge-based electrode were different from its initial cycles due to the formation of SEI layer due to electrolyte decomposition. The CV curves of GeH (**Figure 9a**) and Ge-ene nanosheets (**Figure 9b**) show well aligned redox peaks whereas it is found to be absent in the case of Ge particles (**Figure 9c**), represents different storage of Na-ion process in Ge-ene nanosheets and the GeH (intercalation process) and the Ge-particles (alloying), it is verified through experimental and theoretical procedures. In the initial discharge process, Ge-ene nanosheets (**Figure 9b**) hold a broader peak centred at 0.2 V with a higher current density with larger integrated area in compared to GeH, indicates that there exists a large insertion of Na ions in Ge-ene, which is due to the hydrogen atom removal and creation of abundant active sites for the storage of Na-ions. In subsequent charging phenomena of Ge-ene, there exists two broad peaks present at 0.7 V (first peak) and the 1.1 V (second peak), reflects the deintercalation through multistep procedure of Na ions. In the case of GeH, the CV curve exhibits only single pair of well-defined redox peaks located at 0.005 V under negative scan and 0.7 V for the positive scan. This is due to the presence of hydrogen atom occupation in the active sites or hindering the diffusion of Na ion in GeH. The CV curve of GeH and Ge-ene overlapping perfectly in subsequent cycles, indicates the efficient electrochemical reversibility. The GCD profiles of GeH, Ge-ene nanosheets, and Ge particles are shown in **Figure 9d**. The Ge-ene nanosheets deliver a higher initial discharge capacity of 695 mA h g^{-1} at a current density of 0.1 A g^{-1}, in comparison with GeH (490 mA h g^{-1}) and Ge particles (296 mA h g^{-1}). Ge-ene exhibits an initial Coulombic efficiency of 60.8% whereas it was 48.8% for GeH and 49.6% for Ge particles, demonstrating the reduced irreversible capacity loss and effective cyclic stability of Ge-ene among them. Here, cycling and the rate capability of ultrathin Ge-ene nanosheets, GeH and Ge nanoparticles are depicted in **Figure 9e** and **9f**, respectively. Ge-ene maintains the specific capacity at 315 mA h g^{-1} at a 0.1 A g^{-1} after finishing 50 cycles (**Figure 9e**) and it is greater than GeH (197 mA h g^{-1}) and the Ge nanoparticle (129 mA h g^{-1}). The possession of reduced capacity of Ge-based SIB is due to anode material pulverization during the alloying/dealloying processes, leads to the rapid fading of capacity. Rate capability of 2D Ge-ene nanosheets, GeH, and Ge particles were examined at different current densities such as, 50, 100, 200, and 500 mA g^{-1} and the variations are shown in **Figure 9f**. Ultrathin Ge-ene nanosheets hold higher rate capacity in comparison with GeH and Ge particles and it retained a specific capacity of 342 mA h g^{-1} even at a comparatively higher current density of 500 mA g^{-1}. From these analyses, it can be inferred that the Ge-ene possesses efficient cyclic

View Article Online
DOI: 10.1039/D5SU00085H

capability and rate performance. Ultrathin architecture and higher H-defects induce Ge-ene nanosheet a superior candidate for energy storage application. The 2D ultrathin nanostructure Ge-ene also helped in establishing a more profound interfacial contact between the sheets thereby facilitates electron/ion transportation.

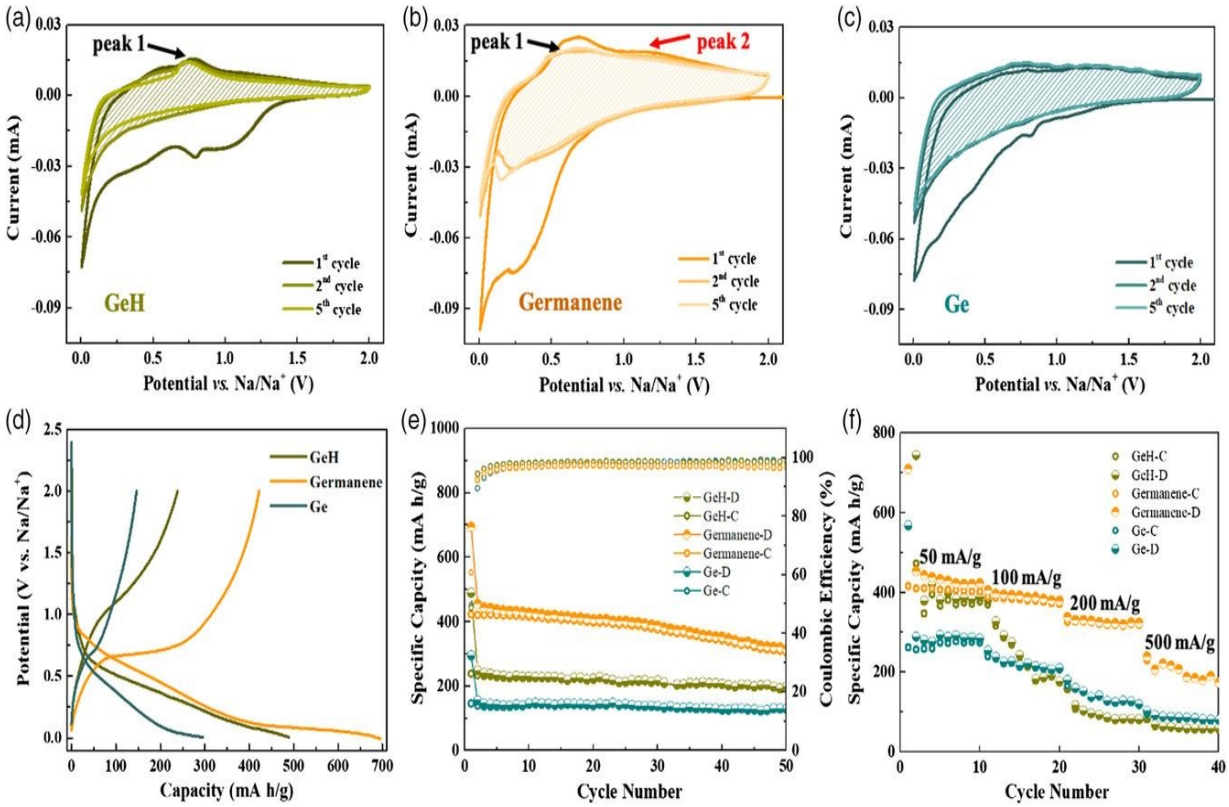

Figure 9. Electrochemical performance evaluations of SIBs. CV curves at 1st, 2nd and 5th cycles for (a) GeH, (b) Ge-ene nanosheets, and (c) Ge particles within a potential window of 0.01 and 2.0 V at a scan rate of 0.1 mV s^{-1}; (d) GCD profiles for the first cycle for Ge-ene nanosheets, GeH, and Ge particles at a current density of 100 mA g^{-1}; (e) Plot of specific capacity and Coulombic efficiency variation at different cycle number of various Ge-based SIBs obtained at a current density of 100 mA g^{-1}; (f) Comparative analysis of rate capability of of various Ge-based SIBs. Reproduced with permission from [45] Copyright (2021) Wiley-Verlag VCH Ltd.

To illustrate charge storage mechanism in defect-rich Ge nanosheets, the authors of this work performed *ex situ* XRD and Raman spectroscopy to understand the sodiation/desodiation phenomena in SIBs. The various charge and discharge states during the CV analysis and GCD measurement of SIB is shown in **Figure 10a** and **b**, respectively. The evaluation on structural change in Ge at various charge and discharge states were examined using *ex situ* XRD, as shown in **Figure 10c**. XRD spectra was recorded for Ge anode in different voltage states as: pristine, 0.2 V (discharge), the 0.005 V (discharge), the 0.8 V (charge), and the 2.0 V (charge) and the different colors represent the various phase composition. For the first stage, peak positioned at 27.8º is introduced from Ge, while peaks located at 43.3º and the 50.4º correspond to Cu foil. While Ge discharged at voltage of 0.2 V (given in the CV curve of **Figure 10a**), no alteration in the XRD pattern was observed. However, when Ge is discharged at a voltage of 0.005 V, the peaks are indexed with hexagonal Ge structure. During charging at 0.8 and at 2.0 V, the diffraction pattern corresponds to Ge and the Cu foil itself. Prominently, local

View Article Online
DOI: 10.1039/D5SU00085H

enlargement in XRD patterns between the peak positions 22º and 32º was deconvoluted into two peaks, which is corresponds to the (002) peak in Ge (blue colour) and the (111) peak in Ge cubic (represented with pink colour), but introduction of the (111) peak in Ge crystal is through partial crystallization during insertion/extraction. In addition to this, (002) peak make a shift towards left during the discharge process due to Na^+ ion intercalation into defect-rich Ge nanosheets, (002) peak make a shift toward right. This proposed that storage of Na ion in Ge is due to the intercalation rather than alloying, which is due to large interlayer spacing in the ultrathin Ge nanosheets that provides enough space for the Na ion migration and transportation. This is confirmed further with *ex situ* Raman spectroscopy (**Figure 10d**). When tuned potential from the OCP toward 0.005 V, the E_{2g} mode is split prominently to two components, having one peak position remain stable and other peak make a shift toward slightly high frequencies. For GeH with hydrogen defects, Na ions do not occupy defect site H among this adsorption, but appearance of the H defect present in material showed a reduced adsorption energy for Na ion, which makes Na atoms stable in the GeH. Here, the highly stable site for the Na atom for metallic Ge is the tetrahedral site (T-site). To evaluate the diffusion of Na ions, the authors utilized climbing image-nudged elastic band (CI-NEB) route for diffusion energy barrier calculation between the proposed sites, shown in **Figure 10e**. Na ions make a diffusion between two nearby SH sites on GeH surface, with two nearby BH sites present for bulk GeH and their two nearby T-sites in the Ge metal as given in **Figure 10f-i**. The Na ions present in Ge possess higher diffusion energy barrier at 0.77 eV. The Na atom have lower diffusion energy barrier in GeH bulk which present at 0.27 eV (in absence of H defect) and at 0.1 eV (in presence of H defect). Here, the presence of H defect leads to a reduction in diffusion energy barrier for Na ions in bulk GeH phase with 0.18 eV and over surface of GeH by 0.06 eV. From **Figure 10f** and **g**, it is clear that appearance of bulk H defect makes an alteration in diffusion path hold by the Na atom. For the Na atom diffusion during the intercalation/de-intercalation process within the Ge-ene nanosheets having H defect is schematically shown in **Figure 10j**.

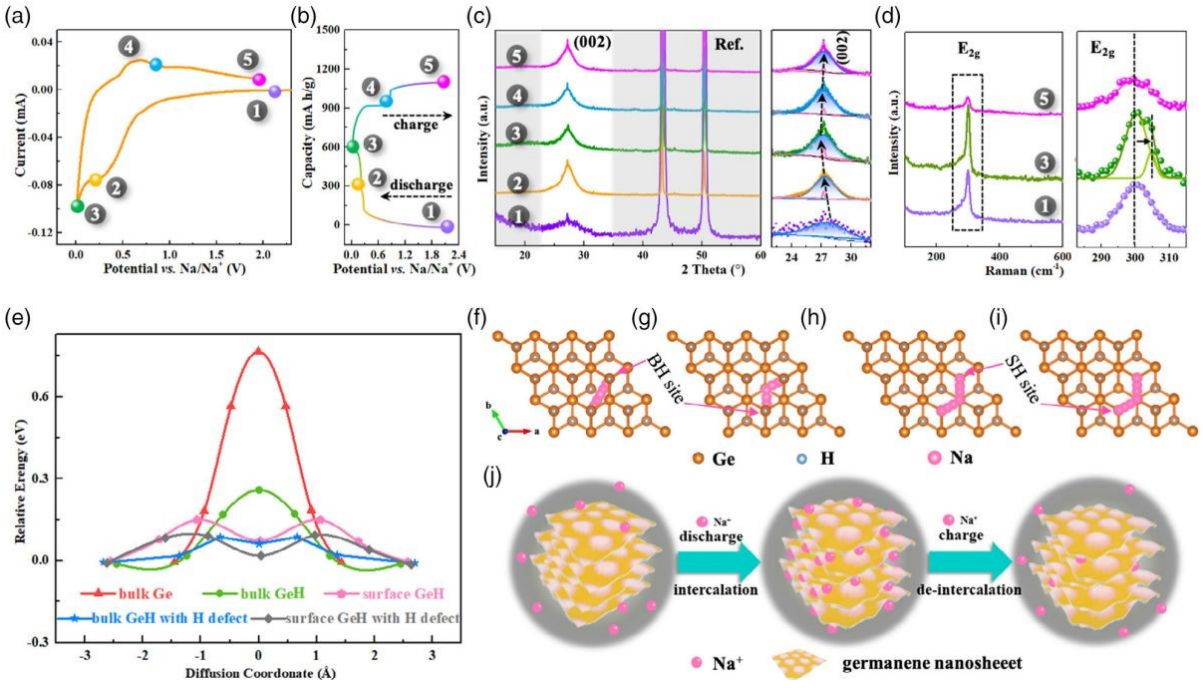

Figure 10. Ex situ XRD, Raman spectroscopy and DFT studies of Ge-ene based SIB. (a) CV curves obtained at a scan rate of 0.1 mV s^{-1} for first cycle within a potential range of 0.005 and 2.0 V; (b) GCD profile; (c) (left panel) *ex situ* XRD pattern at different stages of GCD cycle

View Article Online
DOI: 10.1039/D5SU00085H

and (right panel) a local enlargement of the XRD spectrum showing the peak shift of (002); (d) *ex situ* Raman spectra at different stages of GCD cycle; (e) Diffusion energy barrier comparison for Na adatoms in bulk Ge, bulk GeH, surface GeH, bulk GeH with H defect, surface GeH with H defect; DFT simulated pathways for the Na ion diffusion (f) bulk GeH, (g) bulk GeH with H defect, (h) surface GeH, and (i) surface GeH with H defect (BH: bulk hollow; SH: surface hollow); (j) Pictorial representation of Na ion intercalation in SIBs having Ge-ene anode. Reproduced with permission from [45]Copyright (2021) Wiley-Verlag VCH Ltd.

Buckled architecture hold by Sn-ene is a highly stable candidate in comparison with planar or puckered architecture which possess higher cohesive energy. Using theoretical calculation with spin polarized DFT calculation, it is found that Na atom preferably adsorbed in the hexagonal ring's H site of Sn-ene at a distance of ~ 1.68 Å above perpendicular direction [46]. The adsorption energies calculated is found to be varied upto 0.16 eV/Na atom per each structure. A Bader charge analysis was carried out to the system and found that loss of Na is 0.77 electron per atom electronic charge to the Sn-ene Sn atoms. From this study, it is found that Na adsorption with respect to number of atoms hold highest distortion for Sn-Sn bond length and it is about 5% greater than pristine Sn-ene. These observations were significant enough to use Sn-ene for SIBs with higher efficiency. With the aid of first-principle calculations, a nanomesh structured 2D Sn-ene as an anode material for the SIBs is evaluated by Wu et al. [47]. The nanohole defects present in the Sn-ene improves the binding intensity of Na ion and reducing diffusion barrier of Na as low as 0.15 eV in accordance with the adsorption of Na ion in bulk Sn-ene. This higher nanohole density hold by this nanomesh architecture introduces higher adsorption of Na ions, large theoretical capacity and reduced diffusion barrier. Li-ion interaction on zigzag Sn-ene doped with Beryllium (Be) is evaluated using DFT approach. By taking Be location as a reference, there exists a symmetric structure about Be atom location. Thus, without taking overall hole locations, only nine locations of holes are taken for adsorption energy calculation of Li atom on this Be-doped Sn-ene. The authors of this work observed that with respect to an increase in Li atom adsorption, there occurs a reduction in adsorption energy from the highest value of −2.17 to −1.24 eV. For adsorption of 60th Li atom, the adsorption energy attains a value of −1.24 eV. In addition to this, the open circuit voltage of Be-doped Sn-ene <1.16 eV. Be-doped Sn-ene delivers a storage capacity of 200 mA h g^{-1}, in a case where substrate with all hole locations is occupied with Li atoms. This study introduced an idea about the role of dopants in Sn-ene.

The Zn-air battery is a prominent battery technology with oxygen reduction reaction having slow kinetic performance. Currently, metallenes have received prominent attention as an efficient candidate in Zn-air battery fabrication. By understanding the feature of tetrametallene compounds, Zheng et al. synthesized PdMoCrW tetrametallene having optimized d-band center [48]. For PdMoCrW tetrametallene, high valence metals Mo, Cr and W introduce dissociation of water and it promotes protons for ORR kinetics. In addition to this, the electronic coupling exhibited at the interface of crystalline-amorphous optimizes electronic structure hold by Pd and it attains a downward shift in the d-band center. This makes an attenuation in O adsorption and it increases the ORR activity. The PdMoCrW tetrametallene is synthesized using $(NH_4)_2PdCl_4$, $Mo(CO)_6$, $Cr(CO)_6$, $W(CO)_6$, PVP, CTAB and HCHO is dispersed in DMF solution. After performing stirring, resultant solution is transferred to a Teflon-lined autoclave for a temperature of 150ºC for 12 h. Then resultant product is collected through centrifugation and further washed with ethanol. The resulting PdMoCrW tetrametallene is labelled as $Pd_{75.9}$ $Mo_{9.4}$ $Cr_{8.9}$ $W_{5.8}$. A pictorial illustration of the complete procedure in synthesizing PdMoCrW tetrametallene is shown in **Figure 11a**. Using TEM imaging, the authors of this work found that this tetrametallene having a 2D ultrathin nanosheet morphology (**Figure 11b**). Here, atomic ratio hold by Pd/Mo/Cr/W in this tetrametallene is

View Article Online
DOI: 10.1039/D5SU00085H

75.9:9.4:8.9:5.8. The HRTEM image (**Figure 11c** and **d**) indicates that this tetrametallene consisting of multilayered nanosheets. Here, $Pd_{75.9}$ $Mo_{9.4}$ $Cr_{8.9}$ $W_{5.8}$ tetrametallene nanosheet exhibits a monolayer thickness ranging from 1.41 - 1.49 nm, correspond to 6 - 7 atomic layers. From HAADF-STEM image (**Figure 11e**) and mapping analysis (**Figure 11f-m**), it is found that Pd, Cr, Mo, and W makes a uniform dispersion, agrees with the line scan. The authors evaluated the influence of various experimental parameters on the growth mechanism of tetrametallene. The carbonyl salts pyrolysis introduced CO, which induce formation of nanosheets. Thus, irregularly shaped nanoparticles were introduced in absence of the carbonyl salts. The Br^- ions present in CTAB makes a complex with the metal ions thereby optimizing reduction potential and reduction kinetics. In the absence of CTAB, there are multiple number of polyhedral being introduced over irregular nanosheets, as a result of faster reduction rate. The PVP adsorbed on the surface of metal and spatial cooling introduced by long polymer introduced a spatial-site blocking phenomena thereby preventing the possible agglomeration. Thus, in the absence of PVP, the nanosheets will be agglomerated and leads to the self-assembly to a nanoflower-like morphology. The authors of this work have performed time-dependent experiments in order to understand the formation mechanism of PdMoCrW tetrametallene. Firstly, for an initial time reaction of 1 minute, there exists in the formation of uniformly dispersed Pd nanoparticles. When reaction time reaches to 15 minutes, these Pd nanoparticles formed are tends to aggregate and further nucleates to form small quantity of nanosheets on edge. A further increase in processing time from 15 to 60 minutes, there exists lateral growth of nanosheets with an increase in size and a slow increase in the Mo, Cr, and W content. This process portraits that the Pd nanosheets make a rapid growth and incorporation by these individual elements are slow. When reaction time approaches to 12 h, there is no prominent change in size of nanosheet and a rapid growth of Mo, Cr and W to 9.4%, 8.9%, and 5.8%, respectively, can be observed. This makes an indication on the consumption of Pd precursor in the first 60 minutes, which is followed through interdiffusion and incorporation of Mo, Cr, and W in PdMoCrW tetrametallene. From this study, it can be said that the PdMoCrW tetrametallene is formed via a nucleation−lateral growth−atom diffusion mechanism pathway.

View Article Online
DOI: 10.1039/D5SU00085H

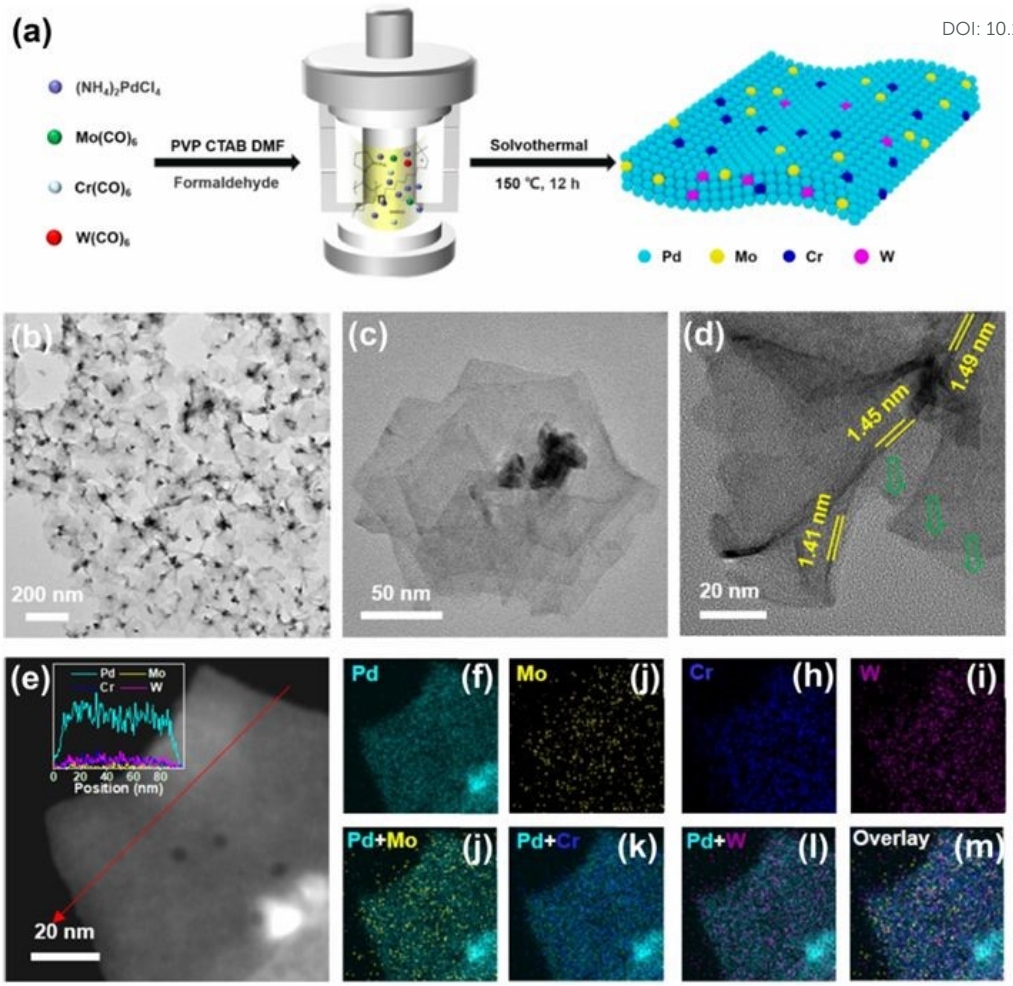

Figure 11. (a) Schematic diagram shows the synthesis procedure of PdMoCrW tetrametallene; (b) TEM image of PdMoCrW tetrametallene; (c and d) HRTEM images of PdMoCrW tetrametallene; (e) HAADF-STEM image (inset image shows the line scan profile along the Red arrow) and (f-m) elemental mapping images. Reproduced with permission from [48] Copyright (2024) American Chemical Society.

For the proposed mechanism, PVP makes a coordination with Pd^{2+} and a reduction in CTAB with formaldehyde in order to produce Pd nanoparticles. In due course, formaldehyde and carbonyl salts decomposed at high temperature in order to produce CO. Basically, CO makes a preferential adsorption on (111) crystal facet present in Pd. If there are enough number of CO molecules to completely cover the Pd surface, it possesses further nanosheets growth along (111) direction of crystal facet and triggers the anisotropic growth towards the formation of metallene. When the reaction time is increased further, there exists a depletion of Pd precursors to stop the nanosheet growth, there exists a gradual incorporation and diffusion of Mo, Cr, and W atoms on the tetrametallene. The authors of this work have performed the electrochemical measurements using tetrametallene with carbon (XC-72) suspension as the working electrode (glassy carbon), the Hg/HgO as a reference electrode and the graphite rod as a counter electrode. The CV measurements were performed in a 0.1 M KOH N_2 saturated solution at a scan rate of 50 mV s^{-1} and the ORR analysis was performed in 0.1 M KOH O_2^- saturated solution at 10 mV s^{-1}. The accelerated durability analysis was performed within a voltage range of 0.6 – 1.0 V vs. RHE at 100 mV s^{-1} for 10000 cycles. From the experimental analysis, it is observed that $Pd_{75.9}Mo_{9.4}Cr_{8.9}W_{5.8}$/C electrode possesses excellent mass and specific activity

of 2.81 mA mg_{Pd}^{-1} at 4.05 mA cm^{-2}, which is found to be higher than the commercial Pt/C. The ORR activity of the metallene is due to the following features: (i) ultrathin 2D metallene curled structure induces a higher density for unsaturated active sites and increases utilization of Pd atom, (ii) synergistic effect of crystalline-amorphous interface facilitates redistribution of charge density and it optimize oxygen intermediates adsorption energy, (iii) intrinsic electronic structure of active sites was optimized with the coordination effect and it is introduced with alloying heteroatoms such as Cr, Mo, and W, and (iv) higher valence state hold by Cr, Mo, and W improves the surface hydrophilicity to the metallene, which accelerates H_2O activation thus provide protons to form OOH*or OH*. In order to perform practical functionality of the prepared catalyst, the authors of this work assembled a Zn-air battery. Two similar Zn-air batteries connected in series combination delivered an open circuit voltage of 2.96 V whereas it was 1.48 V for the single cell (**Figure 12a**). A maximum specific capacity 895 mA h kg_{zn}^{-1} was exhibited by the Zn-air battery, which represents the efficient energy conversion capability (**Figure 12b**). From **Figure 12c**, it is clear that the Zn-air battery exhibited a maximum power density of 156 mW cm^{-2}. The cyclic stability of the battery was tested for 329 h, which shows good stability (**Figure 12d**). This study proposed that the multimetallene architectures are potential candidates for Zn-air battery.

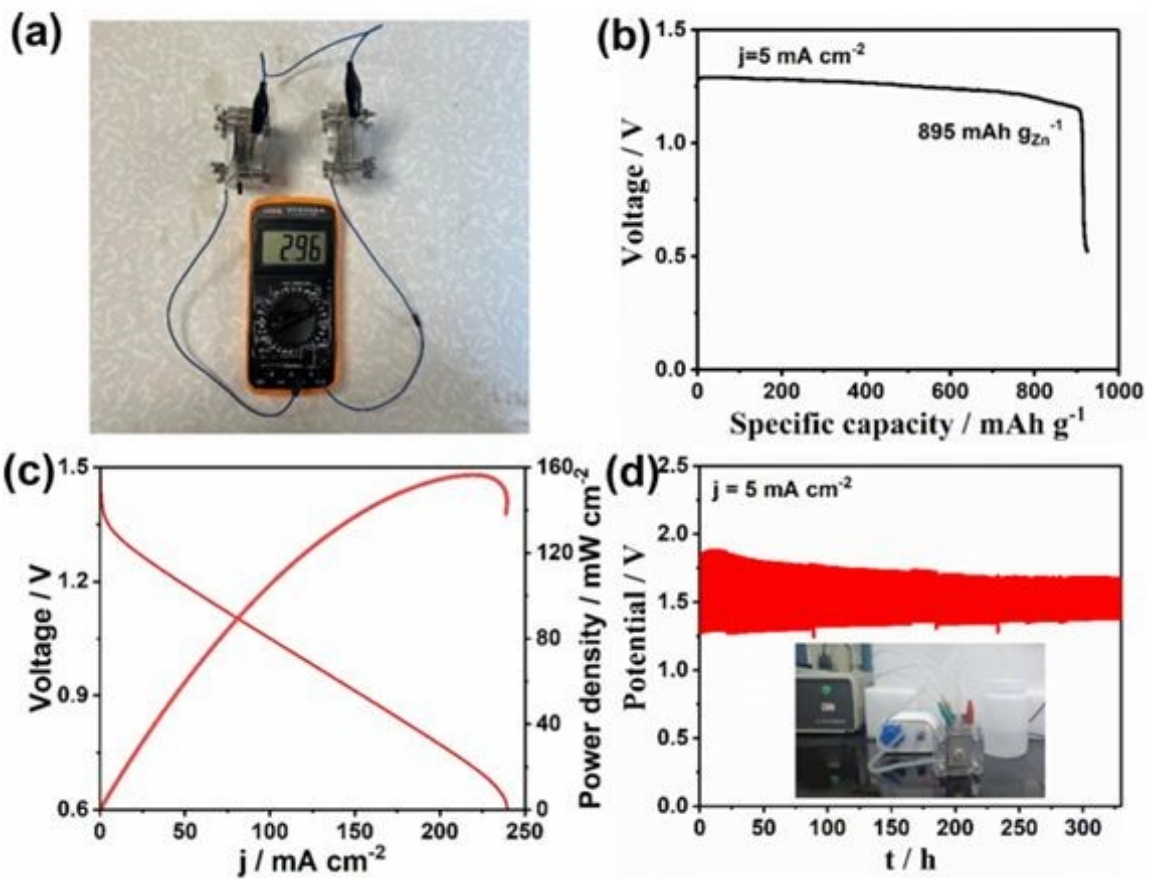

Figure 12. (a) OCV for the series connection of two similar Zn-air batteries tested with a multimeter; (b) Discharge curve at a current density of 5 mA cm^{-2}; (c) polarization curve and power density of Zn-air battery with respect to different current densities; (d) Stability test performed for the Zn-air battery for 329 h. Reproduced with permission from [48] Copyright (2024) American Chemical Society.

View Article Online
DOI: 10.1039/D5SU00085H

With the aid of molecule-metal relay catalysis approach, Zhou et al. [49] introduced rhodium-copper (RhCu) alloy metallene for nitrate conversion toward NH_3 at a low overpotential in a neutral solution. Prominently, the RhCu catalyst has an efficient NH_3 Faradaic efficiency over potential window of −0.1 to −0.4 V. It delivers a maximum NH_3 Faradaic efficiency of 84.8% at reduction potential of −0.2 V in neutral medium, which is found to be higher than pristine Cu and Rh. In addition to this, the authors of this work have demonstrated the assembly of Zn-nitrate/ethanol battery by introducing ethanol in the electrolyte in order to occur ethanol oxidation reaction for boosting energy economy while charging. The Zn-nitrate/ethanol battery exhibited a high energy density of 117364.6 Wh kg_{cat}^{-1} with prominent rate capability with an efficient cycling stability of ~400 cycles. Among the various metallenes, Sb is a potential candidate for rechargeable batteries, due to the buckled hexagonal architecture in the layered form. It is possible to isolate an efficient mono/few-layered Sb through solution phase approach as well as mechanical exfoliation procedure, which delivers higher stability for long-term applications. Using DFT approximations, Sengupta and team [50] evaluated the performance of Na and Li adsorption on free-standing monolayer Sb sheet. The authors of this work have considered a 4 x 4 supercell monolayer Sb for evaluation. In the case of completely sodiated Sb (Na_2Sb), it delivers a high capacity of 320 mAh g^{-1} with a mean operation voltage of ~3.1 eV. Na with a reduced diffusion barrier of 0.114 eV occurs for a path covers adsorption sites having stability at trough of buckle and Γ-point induces efficient charge/discharge rate. For the condition of completely lithiated configuration, LiSb, it delivers a less capacity of 208 mAh g^{-1}, with mean voltage of ~2.0 eV with a large diffusion barrier of 0.38 eV. They observed that in electron density and the electron localization function plot, there exists a potential screening between metal atoms present in 2D Sb, it provides extra stability for lithiated/sodiated structure of Sb favourable for battery applications. Among various rechargeable batteries, Li-sulfur (Li-S) batteries achieved improved performance characteristics when compared to other types. Li-S batteries have profound interest with availability of sulfur in nature, cost-effectiveness, environmentally friendly, and reduced toxicity. But a suitable electrode material is stand as a demerit for its exploration. Allotropes of Sb such as α- and β-phases have semiconducting characteristics having excellent structural stability. Singh et al. [51] studied the disgusting shuttling effect hindering Li-S batteries by using first-principle calculation for α- and β-phases of Sb.

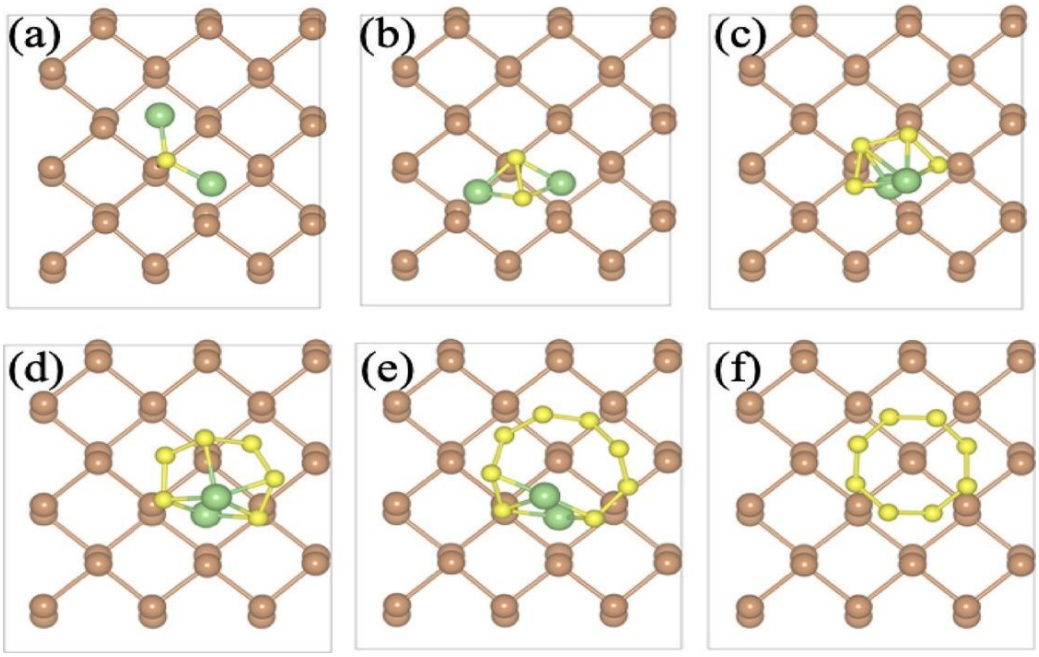

View Article Online
DOI: 10.1039/D5SU00085H

Figure 13. Structure optimized for pristine α-Sb having PBE functional for (a) Li_2S@Sb, (b) Li_2S_2@Sb, (c) Li_2S_4@Sb, (d) Li_2S_6@Sb, (e) Li_2S_8@Sb, and (f) S_8@Sb. Reproduced with permission from [51] Copyright(2021) American Chemical Society.

The authors of this work executed DFT studies with (20 x 20 x 1) k-point for monolayer pristine Sb and the k-point (5 x 5 x 1) for (3 x 3 x 1) and supercell (3 x 4 x 1) α-Sb and the β-Sb monolayer, respectively. Here, Li anode is oxidized and electrons are shifting over to external thread towards cathode and Li ion moving towards the cathode by a porous separator. Further, it reacts with sulfur at different concentration to introduce Li_2S_n (n = 1, 2, 4, 6, and 8) polysulfides. They studied about the LiPS components with α-Sb and β-Sb monolayer and the configuration having good stability are optimized. The structure optimized for pristine α- and β-Sb having PBE functional for Li_2S@Sb, Li_2S_2@Sb, Li_2S_4@Sb, Li_2S_6@Sb, Li_2S_8@Sb, and S_8@Sb are shown in **Figure 13a-f** and **14a-f**, respectively. After optimizing the structures, the vertical distance between the α-Sb and β-Sb surface and the LiPS species >2.0 Å. For Li_2S_n with long chain (n = 4, 6, and 8), Li ions shift at the hollow side of α-Sb and β-Sb surface hexagonal arrangement and there exists a parallel orientation of Sb monolayer. But in short chain (n = 1 and 2), Li ions make a slight displacement from hexagonal orientation of Sb atoms present in the α-Sb and β-Sb, in accordance with the reaction between Li and S atoms. In addition to this, Li atoms bond with Sb atoms of α-Sb and β-Sb with a bond length of ~2.58 Å and Sb to S bond length of 2.58 Å in the Li_2S species short chain. The bond length between Li_2S_2 species and Sb surface is 2.83 and 2.99 Å for Sb-Li and Sb-S, respectively.

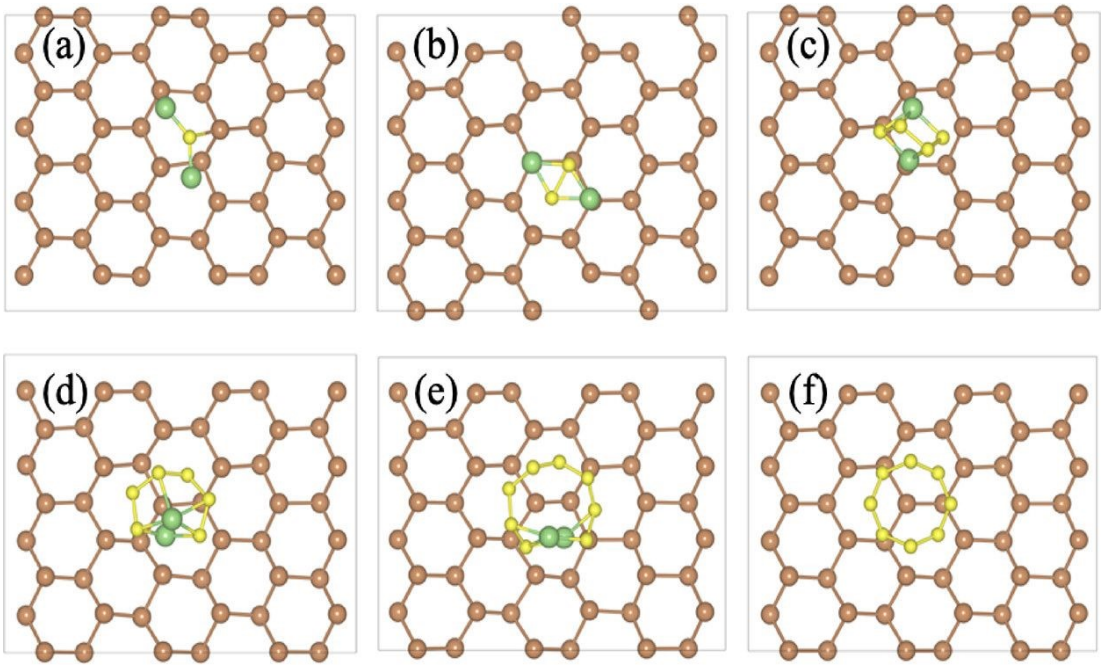

Figure 14. Structure optimized for pristine β-Sb having PBE functional for (a) Li_2S@Sb, (b) Li_2S_2@Sb, (c) Li_2S_4@Sb, (d) Li_2S_6@Sb, (e) Li_2S_8@Sb, and (f) S_8@Sb. Reproduced with permission from [51] Copyright(2021) American Chemical Society.

With the help of DFT simulation, Zhu et al. [52] evaluated about the adsorption features of oxygen-doped Sb monolayer on Li_2S_x species long chain. They observed that with an increase in adsorption energy, oxygen-doped Sb monolayer has higher adsorption of Li_2S_x long chain species in comparison with Sb monolayer. This increased adsorption abstracting the LiPS

View Article Online
DOI: 10.1039/D5SU00085H

dissolution and it preserves the structural integrity of Li_2S_x species. There exists an efficient chemical interaction between Li_2S_x species and oxygen-doped Sb layer. This study reveals the significance of heteroatom doping, particularly oxygen to improve the performance of Sb-based battery systems. The various types of batteries assembled using electrodes comprising of metallenes is tabulated in **Table 1**. In the case of newer generation batteries such as Li-S, potassium-ion batteries, etc., the research is still in infancy. Thus, designing an electrode material using metallenes with proper optimization in the structure and properties are necessary to find their applications in rechargeable batteries to achieve performance, durability, and wide acceptability.

Table 1. Comparison of the electrochemical performances of metallenes-based rechargeable batteries in the literature.

Battery-type	Metallenes used	Synthesis method	Morphology	Major Findings	Ref.
LIB	GeH	Exfoliation	Layered architecture	Capacity: 1180 mA h g^{-1} Coulombic efficiency: 98%	[41]
Zn-CO_2 battery	Sn-ene	Ultrasonication controlled self-assembly	Layered architecture	High power density value of 1.25 mW cm^{-2} at 7.9 mA cm^{-2} current density	[42]
SIB	GeH	Topochemical intercalation with annealing	Ultrathin structure	Discharge capacity: 695 mA h g^{-1} Coulombic efficiency: 60.8%	[45]
Zn-air battery	Trimetallene PdMoCrW	Hydrothermal route	Ultrathin nanosheets	Specific capacity: 895 mA h kg^{-1}	[48]
Zn-air battery	Rhodium-copper alloy metallene	Molecule-metal relay catalysis	Layered nanosheets	Energy density: 117364.6 Wh kg^{-1}	[49]

4. Future Perspectives

By considering an analysis on the metallenes for energy storage systems, it is clear that this new generation 2D material plays an efficient role in sustainable energy storage. The unique properties of metallenes such as large surface area, ultrathin structure, and metallic character make it as an efficient candidate for energy storage applications. The present review critically investigates the real-time applications of metallenes for energy storage applications to find answer for the research question, the energy storage applications of metallenes is a myth or reality. The literature review underlines the potential applications of metallenes for energy storage devices such as supercapacitors, rechargeable batteries, and novel battery systems assembled with the principle of electrocatalytic conversion of chemical compounds. 2D metallenes are not yet explored in a wider platform, thus the utilization of these advanced materials in energy storage systems to compete with the current demand of energy and

View Article Online
DOI: 10.1039/D5SU00085H

sustainability is highly demanded. There exists a limited number of publications, especially the experimental works on the application of metallenes in supercapacitor and rechargeable batteries. Beyond the thermodynamically unfavoured, the isotropic crystalline character in metals make 2D metallenes promising for energy conversion and storage applications. From this review, it is clear that the properties hold by 2D metallenes meet the criteria for energy storage applications hence not a myth. 2D metallenes are potential candidates for exploration in the field of energy storage applications. However, there are some challenges still exists with respect to the widespread exploration of 2D metallenes, which include:

- A suitable unified synthesis approach is mandatory to synthesize 2D metallenes in a facile, low cost, and environmentally friendly manner with higher stability.
- The experimental studies conducted on the application of 2D metallenes for supercapacitors and rechargeable battery application are very less. Mostly, a theoretical perspective of adsorption/desorption of ions, interaction/deintercalation, etc., are explored. Hence it is indeed to conduct more experimental works on this topic.
- Only a limited number of 2D metallenes are explored for energy applications such as Ge-ene, Sn-ene, Sb-ene, etc. It is necessary to develop other possible 2D metallenes and evaluate their potential for energy applications.
- It is necessary to perform advanced characterization analysis for 2D metallenes in order to establish growth and nucleation character and its physiochemical nature. This will help in optimizing the morphology and structure of 2D metallenes.
- In the case of 2D metallenes, only single- and bi-metallene compounds are explored. Similar to these, multimetallic metallenes should be developed such as medium entropy metallenes, high entropy metallenes, etc. and explore their properties for application in energy devices.
- More studies relate to the influence of heteroatom atoms in the crystal structure of 2D metallenes should be undertaken. Doping found to influence the crystal structure as well as the electron energy density, a modulation in the same may helpful in the energy conversion and storage applications.
- Theoretical aspects of defect engineering in 2D metallenes to evaluate their performance modulation for energy conversion and storage applications needs to be explored.
- Studies related to the synthesis of hybrids/heterostructures using 2D metallenes should be undertaken. Carbon nanomaterials [53-55], MXenes [56-58], metal oxide nanostructures [59, 60], etc. are good candidates to prepare hybrid electrodes. The synergistic effects of the individual components in the system will be helpful in achieving the best performance toward energy conversion and storage applications.
- Electronically conducting polymers are best candidates for charge storage due to their excellent pseudocapacitive character [61-63]. Flexible nanocomposites comprising of 2D metallenes and electronically conducting polymers should be prepared for next generation flexible and wearable energy storage devices. This helps in boosting the wide usage of wearable electronic gadgetries which can be as thin as possible.
- A detailed investigation on the comparison of performance of metallenes for novel battery system such as Zn-ion, K-ion, metal-air, etc. are to be explored.
- In-depth analysis on nature of charge storage mechanism in 2D metallenes-based supercapacitors is required. This will help to develop other hybrid supercapacitors with high power and energy densities.

The recently explored studies based on metallenes are mostly the theoretical ones. By considering the above-mentioned facts and by applying suitable modification strategies, it is possible to avoid the current drawbacks of 2D metallenes. There is an urgent need of

View Article Online
DOI: 10.1039/D5SU00085H

exploration of novel 2D metallenes for energy conversion and storage applications since they are promising materials with higher electrochemical stability and promising for durable applications. Although metallenes hold same properties like other ultrathin 2D materials, but research is still in infancy. This is due to the less awareness imparted to the scientific community about this material as well as the difficulty in synthesis approaches to prepare ultrathin 2D structure. There is a great demand for 2D metallenes in the field of physics, chemistry, materials science, energy science and engineering to develop novel devices with properly modulating their properties. The environmentally friendly nature of 2D metallenes helps in replacing other toxic materials for energy conversion and storage technologies which eventually helps in the sustainable development as well the life of our green planet, Earth.

5. Conclusions

We have provided our perspectives on recent developments of energy storage applications of ultrathin 2D metallenes as electrode-active materials in supercapacitors, rechargeable batteries and novel battery systems assembled with the principle of electrocatalytic conversion of chemical compounds. This review unveils the unique properties made them attractive for energy storage applications. The various synthetic strategies adopted to synthesize 2D metallenes such as Ge-ene, Sn-ene, Sb-ene are explored and their energy storage applications are evaluated. However, the other types of metallenes are still in their infancy and need to be developed. Application of 2D metallenes as electrode-active candidates for application in super capacitors and rechargeable batteries are explored with performance evaluations. From our investigation, it can be inferred that the physical, chemical and electrochemical properties of 2D metallenes are important to achieve high performance when using them as electrode candidates in energy storage devices. But there are less reports that describes the charge storage mechanism that can boost the stability as well as electrochemical performance. Multimetallenes are suitable candidates for energy storage applications but still need to be developed. Ultrathin structures make them suitable candidates for electrode application in field of rechargeable batteries and in supercapacitors. Since 2D metallenes possess larger surface area, excellent chemical and electrochemical stabilities coupled with ultrathin layered structure that envisages the rapid movement of electrolyte-ions through it thereby achieves enhanced charge storage due to the diffusion-controlled charge storage. This study exemplary investigated the energy storage applications of 2D metallenes for energy storage applications and hereby declare that the energy storage applications of 2D metallenes are not a myth a reality. By developing ultrathin 2D metallenes are highly advantageous to develop sustainable electrochemical energy storage devices in the future.

Data Availability Statement

The data discussed herein can be found in the referenced articles.

Conflicts of Interest

The authors declare no conflict of interest.

References

1. Thomas, S.A. and J. Cherusseri, *Boron carbon nitride (BCN): an emerging two-dimensional nanomaterial for supercapacitors.* Journal of Materials Chemistry A, 2023. **11**(43): p. 23148-23187.
2. Han, Y., et al., *Recent progress in 2D materials for flexible supercapacitors.* Journal of energy chemistry, 2018. **27**(1): p. 57-72.

3. Bi, W., et al., *MOF-derived ultrathin carbon nanosheets integrated with telluride nanoparticles: synergistic polysulfide adsorption and catalytic sites for enhanced sulfur redox reactions.* Energy & Environmental Science, 2025.
4. Dong, W.-X., et al., *Biomass-derived two-dimensional carbon materials: Synthetic strategies and electrochemical energy storage applications.* FlatChem, 2023. **37**: p. 100467.
5. Thomas, S.A., et al., *Boron carbon nitride (BCN): an emerging two-dimensional material for rechargeable batteries.* Energy & Fuels, 2024. **38**(15): p. 13704-13721.
6. Thomas, S.A., J. Cherusseri, and D.N. Rajendran, *Strategically-designed hierarchical polypyrrole-modified manganese-doped tin disulfide (SnS2) nanocomposite electrodes for supercapatteries with high specific capacity.* Electrochimica Acta, 2024. **504**: p. 144910.
7. Thomas, S.A., J. Cherusseri, and D.N. Rajendran, *Hierarchical two-dimensional layered nickel disulfide (NiS2)@ PEDOT: PSS nanocomposites as battery-type electrodes for battery-type supercapacitors with high energy density.* Electrochem, 2024. **5**(3): p. 298-313.
8. Thomas, S.A., *Layered two-dimensional black phosphorous-based hybrid electrodes for rechargeable batteries.* Journal of Energy Storage, 2023. **73**: p. 109068.
9. Farghali, M., et al., *Strategies to save energy in the context of the energy crisis: a review.* Environmental Chemistry Letters, 2023. **21**(4): p. 2003-2039.
10. Thomas, S.A., et al., *Strategically-Designed Environment-Friendly Tin-Based Electrodes for Sustainable Supercapatteries with High Specific Capacity.* Electrochimica Acta, 2025: p. 145846.
11. Forouzandeh, P. and S.C. Pillai, *Two-dimensional (2D) electrode materials for supercapacitors.* Materials Today: Proceedings, 2021. **41**: p. 498-505.
12. Thomas, S.A., J. Cherusseri, and D. N. Rajendran, *2D nickel sulfide electrodes with superior electrochemical thermal stability along with long cyclic stability for supercapatteries.* Energy Technology, 2024. **12**(6): p. 2301641.
13. Thomas, S.A., J. Cherusseri, and D.N. Rajendran, *Nickel Disulfide (NiS2): A Sustainable Low-Cost Electrode Material for High-Performance Supercapacitors.* Energy Technology, 2024. **12**(7): p. 2400138.
14. Thomas, S.A., J. Cherusseri, and D.N. Rajendran, *Rapid synthesis of hierarchical cobalt disulfide nanostructures by microwave-assisted hydrothermal method for high performance supercapatteries.* ACS Applied Electronic Materials, 2024. **6**(6): p. 4321-4335.
15. Kanimozhi, S.N., et al., *Cu-Zn layered double hydroxides as high-performance electrode for supercapacitor applications.* Electrochimica Acta, 2024. **507**: p. 145106.
16. Thomas, S.A., et al., *Graphitic Carbon Nitride and Their Derivatives*, in *Handbook of Functionalized Carbon Nanostructures: From Synthesis Methods to Applications*. 2024, Springer. p. 1-38.
17. Richard, B., et al., *Minireview on fluid manipulation techniques for the synthesis and energy applications of two-dimensional MXenes: advances, challenges, and perspectives.* Energy & Fuels, 2023. **37**(10): p. 6999-7013.
18. Thomas, S.A. and J. Cherusseri, *A review of Nb2CT x MXene as an emerging 2D material: synthesis, applications in rechargeable batteries and supercapacitors, progress, and outlook.* Energy & Fuels, 2023. **37**(11): p. 7555-7576.
19. Liu, Y., et al., *Metallenes: recent advances and opportunities in energy storage and conversion applications.* ACS Materials Letters, 2020. **2**(9): p. 1148-1172.
20. Liao, M., et al., *Superconductivity in few-layer stanene.* Nature Physics, 2018. **14**(4): p. 344-348.
21. Chu, X., et al., *Pd-Based Metallenes for Fuel Cell Reactions.* The Chemical Record, 2023. **23**(2): p. e202200222.
22. Wang, J. and H.M. Chen, *Metallene pre-catalyst reconstruction for boosting catalytic performance.* Chem Catalysis, 2022. **2**(12): p. 3277-3279.

View Article Online
DOI: 10.1039/D5SU00085H

23. Cao, C., et al., *Metal–organic layers leading to atomically thin bismuthene for efficient carbon dioxide electroreduction to liquid fuel.* Angewandte Chemie International Edition, 2020. **59**(35): p. 15014-15020.
24. Cao, C., Q. Xu, and Q.-L. Zhu, *Ultrathin two-dimensional metallenes for heterogeneous catalysis.* Chem Catalysis, 2022. **2**(4): p. 693-723.
25. Liang, Y., et al., *Current status and future directions of multivalent metal-ion batteries.* Nature Energy, 2020. **5**(9): p. 646-656.
26. Chung, S.H. and A. Manthiram, *Current status and future prospects of metal–sulfur batteries.* Advanced Materials, 2019. **31**(27): p. 1901125.
27. Olabi, A.G., et al., *Metal-air batteries—a review.* Energies, 2021. **14**(21): p. 7373.
28. Thomas, S.A., J. Cherusseri, and D. N. Rajendran, *Rapid Synthesis of Hierarchical Tin Disulfide (SnS2) Nanostructures by a Microwave-Assisted Hydrothermal Method for High-Performance Supercapatteries.* ACS Applied Electronic Materials, 2024.
29. Bhanderi, D., P. Lakhani, and C.K. Modi, *Graphitic carbon nitride (gC 3 N 4) as an emerging photocatalyst for sustainable environmental applications: a comprehensive review.* RSC Sustainability, 2024.
30. Thomas, S.A., J. Cherusseri, and D.N. Rajendran, *Rapid Synthesis of Hierarchical Cobalt Disulfide Nanostructures by Microwave-Assisted Hydrothermal Method for High Performance Supercapatteries.* ACS Applied Electronic Materials, 2024.
31. Cao, C., Q. Xu, and Q.-L. Zhu, *Ultrathin two-dimensional metallenes for heterogeneous catalysis.* Chem Catalysis, 2022.
32. Zhu, Q.-L. and Q. Xu, *Immobilization of ultrafine metal nanoparticles to high-surface-area materials and their catalytic applications.* Chem, 2016. **1**(2): p. 220-245.
33. Xu, Q., et al., *First-principles calculation of optimizing the performance of germanene-based supercapacitors by vacancies and metal atoms.* The Journal of Physical Chemistry C, 2020. **124**(23): p. 12346-12358.
34. Zhu, F.-f., et al., *Epitaxial growth of two-dimensional stanene.* Nature materials, 2015. **14**(10): p. 1020-1025.
35. Zhou, Q., et al., *Quantum capacitance of vacancy-defected and co-doped stanene for supercapacitor electrodes: A theoretical study.* Electrochimica Acta, 2022. **433**: p. 141261.
36. Xu, Y., et al., *Liquid-phase exfoliation of graphene: an overview on exfoliation media, techniques, and challenges.* Nanomaterials, 2018. **8**(11): p. 942.
37. Martínez-Periñán, E., et al., *Antimonene: a novel 2D nanomaterial for supercapacitor applications.* Advanced Energy Materials, 2018. **8**(11): p. 1702606.
38. Girirajan, M., et al., *Two-dimensional layered bismuthene/antimonene nanocomposite as a potential electrode material for the fabrication of high-energy density hybrid supercapacitors.* Energy & Fuels, 2022. **36**(19): p. 12299-12309.
39. Mariappan, V.K., et al., *Antimonene dendritic nanostructures: Dual-functional material for high-performance energy storage and harvesting devices.* Nano Energy, 2020. **77**: p. 105248.
40. Sharma, D.K., et al., *Mono and bi-layer germanene as prospective anode material for Li-ion batteries: A first-principles study.* Computational Condensed Matter, 2018. **16**: p. e00314.
41. Serino, A.C., et al., *Lithium-ion insertion properties of solution-exfoliated germanane.* ACS nano, 2017. **11**(8): p. 7995-8001.
42. Zhang, M., et al., *Few-atom-layer metallene quantum dots toward CO2 electroreduction at ampere-level current density and Zn-CO2 battery.* Chem Catalysis, 2022. **2**(12): p. 3528-3545.
43. Hwang, J.-Y., S.-T. Myung, and Y.-K. Sun, *Sodium-ion batteries: present and future.* Chemical Society Reviews, 2017. **46**(12): p. 3529-3614.
44. Slater, M.D., et al., *Sodium-ion batteries.* Advanced Functional Materials, 2013. **23**(8): p. 947-958.
45. Liu, N., et al., *Germanene Nanosheets: Achieving Superior Sodium-Ion Storage via Pseudointercalation Reactions.* Small Structures, 2021. **2**(10): p. 2100041.

View Article Online
DOI: 10.1039/D5SU00085H

46. Swarup, A., *Electrochemical properties of stanene as an efficient anode material for Na-ion batteries.* Computational Condensed Matter, 2018. **14**: p. 84-88.
47. Wu, L., et al., *Stanene nanomeshes as anode materials for Na-ion batteries.* Journal of Materials Chemistry A, 2018. **6**(17): p. 7933-7941.
48. Zheng, Z., et al., *Crystalline–Amorphous Heterophase PdMoCrW Tetrametallene: Highly Efficient Oxygen Reduction Electrocatalysts for a Long-Term Zn–Air Battery.* Langmuir, 2024. **40**(21): p. 11307-11316.
49. Zhou, J., et al., *Constructing molecule-metal relay catalysis over heterophase metallene for high-performance rechargeable zinc-nitrate/ethanol batteries.* Proceedings of the National Academy of Sciences, 2023. **120**(50): p. e2311149120.
50. Sengupta, A. and T. Frauenheim, *Lithium and sodium adsorption properties of monolayer antimonene.* Materials Today Energy, 2017. **5**: p. 347-354.
51. Singh, D., et al., *Antimonene allotropes α-and β-phases as promising anchoring materials for lithium–sulfur batteries.* Energy & Fuels, 2021. **35**(10): p. 9001-9009.
52. Zhu, V. and X. Luo, *Oxygen-doped antimonene monolayer as a promising anchoring material for lithium–sulfur batteries: a first-principles study.* RSC Advances, 2023. **13**(43): p. 30443-30452.
53. Thomas, S.A., J. Cherusseri, and D.N. Rajendran, *Recent progresses in the synthesis and strategic designs of sustainable carbon-based fibrous electrodes for flexible batteries.* RSC Sustainability, 2025. **3**(1): p. 219-242.
54. Thomas, S.A., J. Cherusseri, and D.N. Rajendran, *Recent advancements on carbon fibers-based sustainable electrodes for flexible and wearable supercapacitors.* RSC Sustainability, 2024.
55. Thomas, S.A., J. Cherusseri, and D.N. Rajendran, *Functionalized Carbon Nanostructures for Hydrogen Storage*, in *Handbook of Functionalized Carbon Nanostructures: From Synthesis Methods to Applications*. 2024, Springer. p. 1471-1509.
56. Zaed, M., et al., *Utilization of recycled materials for low-cost MXene synthesis and fabrication of graphite/MXene composite for enhanced water desalination performance.* Separation and Purification Technology, 2025. **354**: p. 129055.
57. Zaed, M., et al., *Synthesis of Ti3C2Tx MXene@ Carbon-Enhanced cellulose fiber composite-based photothermal absorber for sustainable water desalination.* Materials Today Sustainability, 2024. **28**: p. 100971.
58. Zaed, M., et al., *Unlocking desalination's potential: Harnessing MXene composite for sustainable desalination.* Chemical Engineering Journal, 2024. **500**: p. 156910.
59. Pallavolu, M.R., et al., *Scalable synthesis of binder-free hierarchical MnCo2O4 nanospikes/Ni (OH) 2 nanosheets composite electrodes for high-capacity supercapatteries.* Journal of Energy Storage, 2023. **73**: p. 108999.
60. Thomas, S.A., J. Cherusseri, and M. Khalid, *A comprehensive review on tungsten oxide nanostructures-based electrochromic supercapacitors and machine learning models for design and process parameter optimization.* Energy Storage, 2023. **5**(8): p. e499.
61. Cherusseri, J. and K.K. Kar, *Recent progress in nanocomposites based on carbon nanomaterials and electronically conducting polymers.* Polymer nanocomposites based on inorganic and organic nanomaterials, 2015: p. 229-256.
62. Cherusseri, J., et al., *Polymer-based composite materials: characterizations.* Composite materials: processing, applications, characterizations, 2017: p. 37-77.
63. Thomas, S.A., J. Cherusseri, and D.N. Rajendran, *A Minireview on Polyurethane-Based Flexible Electrodes for Wearable Supercapacitors: Strategies, Syntheses and Electrochemical Performance Evaluations.* Energy & Fuels, 2024. **39**(1): p. 2-18.

The data discussed herein can be found in the referenced articles.

View Article Online
DOI: 10.1039/D5SU00085H